Master thesis

On

Interseismic deformation of two major active faults in eastern Iran: contribution of satellite radar interferometry (InSAR)

Supervision by:

Erwan Pathier and Andrea Walpersdorf

Prepared by:

Zahra Mousavi

Master Student of Erasmus Mundus program at

University of Joseph Fourier, Grenoble, France

Rose School, Pavia, Italy

2009-2010

Submitted in June 2010

Acknowledgements

I wish to thank Erwan Partier for his experience, availability and useful technical advice that helped me to acquire scientific rigor and a methodology that will allow me to continue successfully on this research path. My deepest gratitude goes to my advisor Andrea Walpersdorf for her supporting, advice, encouragement and kindness.

I particularly thank Cécile Lasserre who helped me to learn about InSAR software. She was always patient about my question and made me feel free to ask questions. I wish to thank Isabelle Manighetti for her help in the tectonic part of the dissertation and for sharing her fault trace catalogue.

This work has been done in the Laboratoire de Géophysique Interne et Tectonophysique (LGIT) to complete the MEEES program in Engineering seismology. I would like to thank them in supporting me to study in Italy and France. I wish to thank specially the director of LGIT, Fabric Cotton and his colleague Stéphane Garambois for their kindness and hospitality during my education.

I like to thank Mr Tavakoli who encouraged me to continue my education and make the environment easy for me to come to Europe. Also I wish to thank the whole of my colleagues at National Cartography Center.

I know I cannot be here without my family supporting, love and concern. My heartfelt thanks for their hospitality and to make me feel I am not alone anytime.

Abstract

Published slip rates on major faults in Eastern Iran show discrepancies especially between the GPS interseismic slip rates (less than 1mm/yr on the Doruneh fault) and geological slip rates (2.4±0.3mm/yr). In both approaches measurements are very sparse. This motivated us to use the space-borne radar interferometry (INSAR) technique which has the potential to improve the spatial coverage and resolution of interseismic measurements and then to help us to resolve some open questions concerning the fault mechanisms, the seismic hazard they present, and the role they are playing in the regional tectonics. This study focuses on two active faults, the Doruneh and Dasht-e-Bayaz faults using radar image from the ENVISAT satellite. For the studied region the data archive cover the period 2003-2010. We select the eastern part of the Doruneh fault as our target area (crossed by the descending tracks, 392 and 435). 16 interferograms for Track 392 and 22 interferograms for track 435 have been processed using the ROI_PAC software. The visual examination of individual interferograms combined with an active faults map indicates that there is no significant superficial creep (i.e. > 1mm/yr) on the Doruneh and Dasht-e-Bayaz Faults during the examined period 2003-2007. To investigate the long wavelength interseismic tectonics signal, we used a simple stacking approach in order to enhance the deformation signal with respect to atmospheric effect and orbital errors. Averaged InSAR measurement profiles are constructed along track (North-South). These 300km long profiles cross the Doruneh and Dasht-e-Bayaz faults in track 392 and only the Doruneh fault in track 435. The comparison of these profiles to synthetic profiles derived from simple dislocation model for elastic interseismic deformation, shows that the signal to noise ratio of the InSAR measurement is too low to be able to detect the tectonic signal. The limits of our interferogram dataset and of the stacking approach do not allow us to separate the tectonic signal from the remaining other sources of error (unwrapping error, orbital error and atmospheric effect). New data but also a more sophisticated interferogram analysis are needed to increase the signal to noise ratio. For example, the so-called “Small baseline” approach coupled with atmospheric correction using GPS observations or meteorological models could be used in future work.

Résumé

Les taux glissements publiés sur les failles actives dans l'Est de l'Iran montre des différences significatives notamment entre les taux issus de mesures GPS (indiquant moins d'un mm/an sur la faille de Doruneh) et ceux issus des études géologiques (2.4±0.3mm/yr). Toutefois, dans les deux cas, ces mesures sont très ponctuelles. Ce travail cherche à améliorer la couverture spatiale et la densité des mesures de déformation dans la région en utilisant la méthode de l'interférométrie radar différentielle satellitaire avec pour objectif de répondre à plusieurs questions encore ouvertes sur le fonctionnement des failles actives dans le Nord-Est Iranien, sur leur rôle dans la tectonique régionale, ainsi que sur l'aléa sismique qu'elles représentent. Cette étude se penche plus particulièrement sur deux failles actives majeures de la région : la faille de Doruneh et celle de Dasht-e-Bayaz, en utilisant des images radar acquises par le satellite ENVISAT. Sur la région étudiée l'archive de données couvre la période 2003-2010. La partie Est de la faille de Doruneh (couverte par les passes descendantes du satellite n°392 et 435) a été choisie comme cible d'étude. Seize interférogrammes pour la passe 392 et vingt-deux pour la passe 435 ont été réalisés à l'aide des programmes ROI_PAC. L'examen visuel des interferogrammes individuels couplés à la carte des failles actives montre qu'il n'y a pas de fluage superficiel localisé supérieur au mm/an sur les deux failles étudiées durant la période 2004-2010. Afin d'examiner la déformation tectonique intersismique à grande longueur d'onde, une méthode simple dite de « stacking » a été employée dans le but de renforcer le signal tectonique par rapport aux signaux liés à l'atmosphère et aux erreurs orbitales. Des profils moyens Nord-Sud de mesures de vitesse INSAR ont été réalisés. Ces profils d'environ 300km de long passent au travers les failles de Doruneh et Dasht-e-Bayaz sur la passe 392 et seulement sur la faille de Doruneh sur la passe 435. La comparaison de ces profils avec des profils synthétiques produits à partir d'un modèle simple de déformation à base de dislocation dans un milieu élastique, montre que le rapport signal à bruit des mesures INSAR est trop faible pour permettre la détection du signal tectonique. En effet, les limites du jeu d'interférogrammes calculés et celle de l'approche par « stacking » font qu'il n'est pas possible de séparer le signal tectonique des sources d'erreurs (erreur de déroulement de phase, erreurs orbitales, effet atmosphériques). Toutefois, l'arrivée de nouvelles données, mais surtout l'utilisation de méthode d'analyse plus sophistiquée, telle que l'approche dite « small baseline analysis» couplée à des corrections atmospheriques basées sur des observations GPS ou des modèles atmosphériques, pourrait permettre d'atteindre les précisions de mesures requises dans le cadre de futurs travaux.

Table of Contents

1 Introduction

The large tectonic activity creates high seismicity in Iran, with large and shallow destructive earthquakes as many have been recorded in the last century. Active tectonics in Iran is related to the Arabian-Eurasian convergence, taking place inside the political borders of this country. The part of the convergence that is not absorbed in Zagros at its SW border must be accommodated as shear between the Central Iran and the Helmand sub-plate to the east of Iran. This is creating a significant amount of NS shear in eastern Iran. The tectonic deformation in eastern Iran is localized mainly on NS oriented right-lateral faults surrounding the aseismic Lut block, and EW left-lateral fault at the northern boundary of the Lut block. These faults have a crucial role in accommodating the NS shear. They produce large earthquakes like Tabas (1978) and Bam (2003) and are a large source of seismic hazard. Several important questions about the tectonics of Eastern Iran remain unsolved: which part of the shear rate is accommodated on the east and west boundaries of the Lut Block to know how much is absorbed on the northern faults. What are their roles in the tectonic mechanism with respect to long term and short term behavior? Does the present and past behavior of these faults confirms the need of block rotation models to be consistent (e.g. Walker and Jackson, 2004)? If yes, what is the role of such a rotation for the initiation of new faults in eastern Iran? Why do some of these faults experience more earthquake than others, like Dasht-e--Bayaz with 3 large earthquakes in 40 years, and Doruneh, 200 km apart, with 700 km length and no important earthquake? To address these questions, it is needed to combine short term and long term measurement. Long term measurements like geology and geomorphology and short term observations such as geodesy (GPS network) help to have a complete view of the ongoing tectonic activity.

In this study, we will focus on the Doruneh and the Dasht-e-Bayaz faults as examples of individual faults in the northern part of Lut Block. For these target faults, short term and long term measurements like a GPS network and geomorphology and geology studies are available. We want to complete these studies by measurements of the instantaneous interseismic deformation field by InSAR. Although the estimated fault velocity are very low (mm/year) and then difficult to measure, the Doruneh and Dasht-e-Bayaz faults have favorable orientations (roughly East-West) for InSAR measurements. Furthermore, the faults cut through an arid environment limiting temporal decorrelation in interferograms that has

been shown in previous studies using InSAR on earthquake or subsidence phenomena (Funning et al., 2005; Parsons et al., 2006; Motagh et al., 2008; Fielding et al., 2009).

The 700 km long Doruneh fault is one of the most prominent faults in east of Iran. It is oriented east-west (see figure 2.1). This fault accommodates the 15 mm/yr of north-south right-lateral shear between central Iran and Afghanistan by vertical axis clockwise rotation (Walker and Jackson, 2004). The geomorphological offsets across the Doruneh fault contain numerous indications of cumulative left-lateral slip over various scales and its slip rate is estimated to 2.4 ± 0.3 mm/year by luminescence dating (Fattahi et al., 2006). Until now, no large earthquake has been recorded on this fault. However, if we consider a scale relationship (Sholz, 1982; Wells & Coppersmith, 1994) between the length of a fault and the recurrence time of its ruptures, this fault has a recurrence time for large earthquakes (7.7) every ~2000 yr. Several GPS stations have been established to measure the present-day slip rate of this main fault in east of Iran. While in the west part of the fault, the number of stations is too small to be able to estimate the slip rate in the east part of the fault, a maximum left-lateral slip rate of 1 mm/yr is determined (Walpersdorf et al., 2010).

The GPS measurements show the same low slip rates (less than 1 mm/yr) for the Dashte-Bayaz fault (Walpersdorf et al., 2010), but the Dasht-e-Bayaz fault, in contrast to Doruneh, experienced high recent seismicity. Berberian & Yeats (1999) estimated average slip rate about 2.5mm/yr base on the line of Qanats.

To better understand the fault activity the knowledge of the slip rate variation along the fault is an important issue. To address this question, several dense GPS profiles across the fault would be needed. The set up of such a GPS network in this area is difficult because of security and political reasons. The present work aims at taking advantage of the remote sensing capabilities of Interferometric Synthetic Aperture Radar (InSAR) to make the measurement spatially more dense around the fault and then to be able to make several profiles across it. The large coverage, convenient image resolution and the acceptable precision of InSAR make it a powerful technique for studying geologic events like earthquakes, subsidence and landslides. More precisely, InSAR technique has proved to be able to measure interseismic slip rate on several continental strike-slip fault (e.g. Wright et al., 2001; Cavalié et al., 2008) similar to the Doruneh fault. The major difficulty lies in the fact that the Doruneh fault seems to have low slip rate (1 to 3 mm/year), at the limits of the InSAR measurement capabilities considering the available ENVISAT archives. Nonetheless, the Doruneh fault presents several advantages: In comparison to other places in Iran, where faults appear in clusters, inside which possible interactions can be difficult to unravel, Doruneh is a rather isolated fault, making it simpler to analyze.

South of the Doruneh fault, the study of the Dasht-e-Bayaz fault could also benefit from the InSAR investigation. Its present-day slip rate estimated from GPS is at most 1.5±2

mm/yr (Tavakoli, 2007) or even less than 1 mm/yr after repeat measurements (Walpersdorf et al., in preparation), which is clearly less than the proposition of 2.5 mm/yr by Berberian and Yeats (1999) and Walker and Jackson (2004). However, this fault is seismically active. During the 1968 August 31 Dasht-e-Bayaz earthquake (Mw=7.1), a left-lateral displacement of 2.5 m was observed (Tchalenko et al., 1973)

In summary, the contrast between short term measurement (GPS) and long term measurement (geomorphological and geological) proposes us to think about the mechanism of absorbing the strong NS shear at the northern Lut block boundary. The absence of significant left lateral slip on the two prominent faults indicates that the NS shear accommodation changes its behaviour in time (or that it is slower than what the geological methods predict). In this step using other geodetic methods like the InSAR technique seems to be necessary to have a better interpretation of these differences between geodetic and short term geologic slip rates. Therefore, the InSAR technique helps to find the discrepancy between geological and geodetic slip rates on Dasht-e-Bayaz fault, and between geomorphological expression and GPS slip rate on Doruneh fault. The open questions are:

- Is the InSAR short term slip rate across these two faults confirming the GPS rate or the geological rate?
- Does InSAR by its continuous spatial coverage locate the deformation in other places than the discontinuous GPS network?
- Does the combination of GPS and InSAR measurements permit to explain the geologic slip rate? If not, does it mean the simple interseismic model does not properly work? Can we constrain a different model than an elastic model? Or are the geological rates overestimated?

In the following, the kinematic background of the target faults (chapter 2) and the method and the capacities of InSAR for the measurement of a deformation field are presented (chapter 3), then some preliminary results of the InSAR measured displacement field in eastern Iran are given (chapter 4).

2 Iran tectonics

Active tectonics of the Iranian plateau is dominated by the convergence between the Arabian and Eurasian plates. GPS observations show approximately north-south shortening in eastern Iran, with rates increasing eastward, from about 20 mm/yr at 50˚E to 26 mm/yr at 60˚E (Vernant et al., 2004). This amount is less than the rates from global plate tectonic models (NUVEL1-A, DeMets et al., 1994), constrained by the analysis of global seafloor spreading.

The Arabia-Eurasia convergence is accommodated differently in the eastern and the western part of Iran, with oceanic subduction in the Makran in the east, and continental collision in the Zagros and Alborz mountain belts in the west as major mechanisms (Vernant et al., 2004). The part of the shortening that is not taken up in Zagros yields the northward motion of Central Iran. This residual motion causes an N-S right-lateral shear between central and eastern Iran and Afghanistan further east.

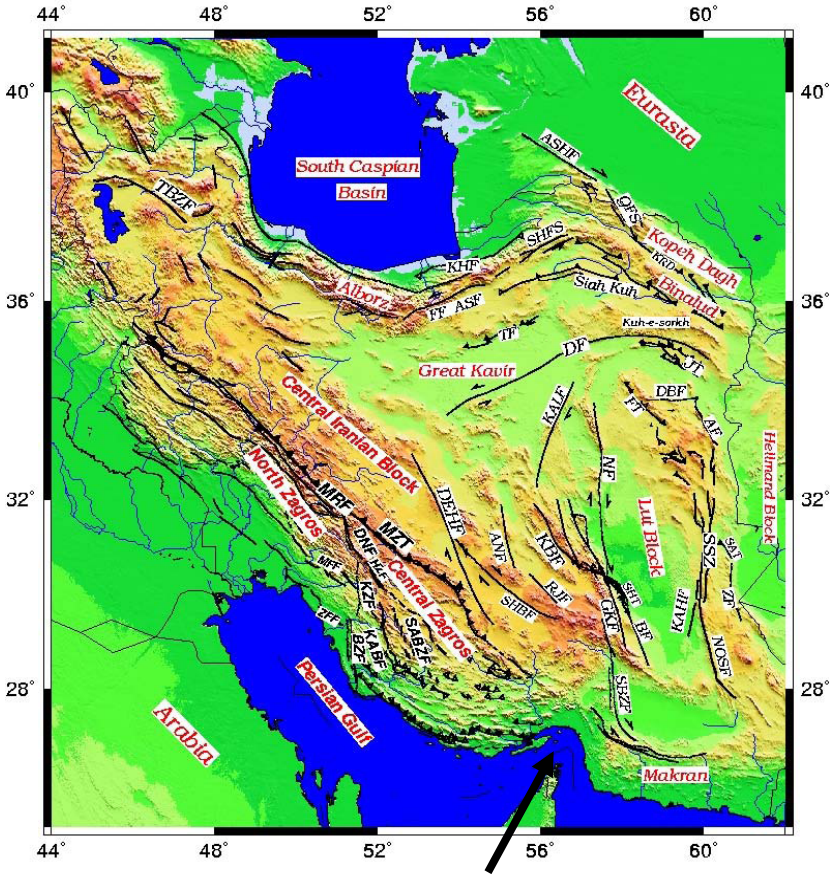

Figure 2.1 : Principal active faults of Iran. Faults are represented by black lines (DF: Doruneh Fault, DBF: Dashte-Bayaz Fault) superimposed on a shaded DEM. The Arabia-Eurasia convergence is shown by the black arrow which is close to 22mm/yr.

The right lateral shear in eastern Iran is taken up on two north-south strike-slip fault systems located on each side of the Dasht-e Lut block which is flat, low lying and aseismic

(Walker & Jackson, 2004). This shear is accommodated in the western part by the Gowk-Nayband fault system, and in the eastern part by the Sistan suture zone with the Neh-Abiz-Zahedan fault systems. But north of ~34˚, the right-lateral shear is accommodated on EW oriented left-lateral strike-slip faults such as Doruneh and Dasht-e-Bayaz faults that are supposed to rotate clockwise about vertical axes (Jackson and McKenzie, 1984).

2.1 Doruneh fault

The Doruneh left-lateral strike slip fault is one of the longest faults in Iran. It extends from the border of Afghanistan to the central Dasht-e-Kavir desert in central Iran. This fault performs an important role in accommodating right-lateral shear in eastern Iran (Figure 2.1).

The left-lateral Doruneh fault was first named by Wellman (1966). The western part is often called the Great Kavir fault (Figure 2.2-1). This fault is trending east-west but there is a prominent curvature in the Doruneh fault trace, with an ESE–WNW strike in the east that bends round to a WSW–ESE strike west of ~58˚E (Walker & Jackson, 2004). The Doruneh fault accommodates part of the 15 mm/yr of north- south right-lateral shear between Iran and Afghanistan (Vernant et al. 2004), so it must rotate clockwise about a vertical axis in order to accommodate this shear (Jackson & McKenzie, 1984).

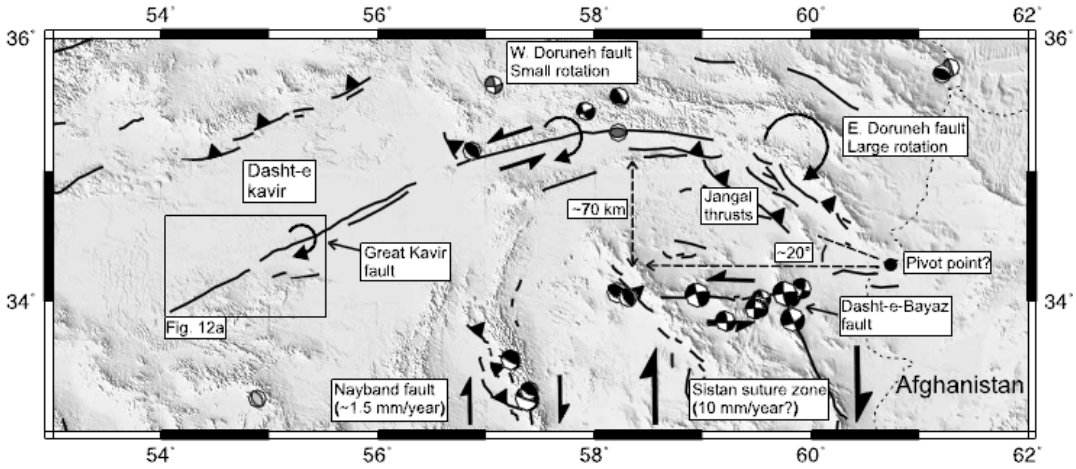

Figure 2.2: Map of active faults in North-East Iran with fault-plane solutions of recent earthquakes and with kinematic model indications and long term slip rates. Background is shaded topography from GTOPO30. The Doruneh fault is made of several segments (Great Kavir, W Doruneh fault, E Doruneh fault). The Nayband and Dasht-e-Bayaz faults are located southward. According to Walker tectonic model, the arrows show how N–S right-lateral shear that can be accommodated by clockwise rotation about vertical axes of blocks with left-lateral strike-slip faults at their edges by west to east imigration. (From Walker et al., 2004).

Four historical earthquakes happened in the Doruneh fault area in 1336AD, 1619, 1903 and 1923 (Ambraseys & Melville, 1982). Only the 1903 and 1923 historical earthquakes

can be attributed directly to the Doruneh fault. This region experienced also 5 instrumental earthquakes in the 19th century. According to the epicenter coordinates, only one of the instrumental earthquakes is close to the Doruneh fault, while the others are located on the Kuh-e Sorkh fault system. Thus this fault seems to have low recorded seismicity.

Satellite imagery helps geologists to identify fault offsets. Clear scarps in alluvial fans and river terraces are seen along the entire Doruneh fault length and can be observed both in satellite imagery and in the field. Fattahi et al. (2006) Indicated 3 places where the lateral displacement on this fault can be quantified and dated. These places are Uch Palang, Kuh-e Teagh Ahmad and Shesh-Taraz. He estimates the slip rate is 2.4±0.3mm/yr in Shesh-Taraz Rivers.

Geodetic instantaneous slip rates are obtained by the Iranian permanent GPS network and GPS campaign networks in eastern Iran such as the Kerman and Kopeh-Dagh networks. Figure 2.3 shows the velocity field of this region with respect to Eurasia.

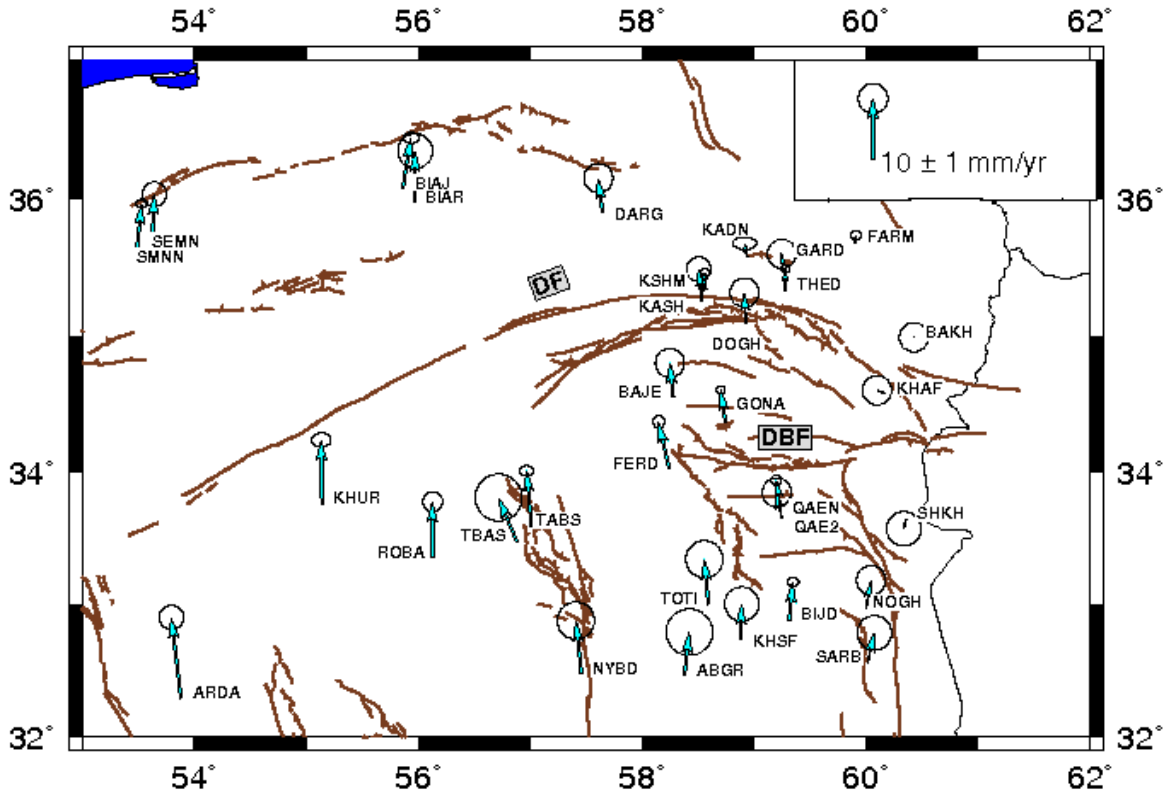

Figure 2.3: East Iran velocity field with respect to Eurasia surrounding Doruneh Fault (DF) and Dashte-Bayaz Fault (DBF), Note the less than 1mm/yr variation in GPS velocity crossing these faults. (Walpersdorf et al., 2010)

The GPS stations surrounding the Doruneh fault show a regional kinematic pattern that varies with longitude along the fault trace, without indicating significant left-lateral present-day slip of the Doruneh fault itself. East of 60˚E, the velocity of two sites BAKH and KHAF north and south of the eastern Doruneh fault trace show a slight component of right-

lateral slip and 0.5 mm/yr shortening across the Doruneh fault. Further west (longitudes 58˚-60˚) is a rigid unit characterized by the stations GONA-BAJE-DOGH situated south of the fault. With respect to this rigid unit, the four stations THED, GARD, KADN and FARM to the north of the fault show mainly NS shortening across the fault trace. West of 58˚, a relatively distant site indicates only very weak displacements across the fault, and in particular no more shortening is observed across the Doruneh fault trace. Even further west (<56° E), there is no close site anymore to monitor the slip rate of this fault (Walpersdorf et al., 2010).

2.2 Dashte-Bayaz Fault

The Dasht-e-Bayaz fault is an E-W trending left-lateral fault system located to the north of the Lut block at latitude 34°N. This fault consists of one 70-km-long west segment that ruptured in 1968 (Ms 7.4) and one 50-km-long east segment that ruptured 11 yr later (1979, Ms 7.1). The two segments of the Dasht-e-Bayaz fault are separated by the N-S trending right-lateral Mahyar fault (Berberian & Yeats, 1999). Berberian & Yeats (1999) used offsets based on the line of Qanats (underground water channel) to find the average slip rate about 2.5mm/yr, assuming that these Qanats have a maximum age of 4000 years.
Several large historical and instrumental earthquakes larger than magnitude 7 took place on Dasht-e-Bayaz fault (Figure 2.2). The Dasht-e-Bayaz seismicity presents a clustering of earthquakes in the 20th century. 3 major earthquakes took place in the last 40 years in this region including the two magnitude 7.1 events in 1968 and 1979 rupturing the western and eastern segment of the DBF. Another magnitude M_w 7.2 earthquake took place in 1997 on the Abiz fault connecting to the DBF at its eastern extension (Fig. 2.2)

Figure 2.3 shows the velocity field for Dasht-e-Bayaz with respect to Eurasia (left) and with respect to GONA station (right). South of DBF the two sites QAEN (permanent station) and QAE2 (campaign site on bedrock) show coherent velocities that are also of small amplitude. In particular, they have no significant east component that would correspond to the present-day left-lateral strike-slip activity of the DBF.

The two prominent left-lateral strike-slip faults bordering the Lut block to the north, the DF and the DBF, do not present instantaneous slip rates that are detectable with the available GPS measurements. The major deformation mechanism at the northern Lut block limit seems to be shortening across oblique thrust faults (Walpersdorf et al., 2010)

2.3 Tectonic model and slip rate comparison

According to Walker and Jackson (2004), the left-lateral Doruneh fault is expected to accommodate a part of the NS shear between central Iran and Afghanistan increasing from

west to east (see Figure 2.2). They suggested a simple model that N–S shear is accommodated by clockwise rotation about vertical axes of fault-bounded blocks. The total fault offset (4–5 km) caused by rotation in Figure 2.2 varies with the width of the rotating blocks. That means that the left-lateral slip and clockwise rotation of the Dasht-e-Bayaz fault has not accommodated a large amount of the expected 50-70 km of N–S right-lateral shear between central Iran and Afghanistan. The Dasht-e-Bayaz fault must therefore either be relatively unimportant in accommodating right-lateral shear in eastern Iran, or must be a relatively young feature. The authors observe that the Dasht-e-Bayaz fault occurs only across the region east of longitude 58◦E, where the Doruneh fault system becomes perpendicular to the NNE–SSW regional convergence. The eastern part of the Doruneh fault can no longer rotate away from the direction of regional shortening. This situation may have caused the initiation of a new strike-slip fault across this region. But west of longitude 58◦E, the Doruneh fault is still able to rotate clockwise and accommodate right-lateral shear, and so no new fault has been initiated here.

Finally, the comparison of slip rates from the GPS analysis with short and long term geologic slip rates helps to identify the role of the Doruneh and Dasht-e-Bayaz faults in the regional tectonic mechanism and in particular in the present-day kinematics. We have to keep in mind the difference between these three rates. There are two types of geological slip rate estimates, one over the long term from total geological fault offsets and an estimated age of regional deformation onset (generally thought to be 5-7 Ma in Iran), and one over the short term from geomorphological marker offsets created by an active fault and dated (by different strategies) over some thousand to tenths of thousand years. The geodetic slip rates are obtained by measuring geodetic marker offsets over a few years. Each method provides average slip rates over the respective time span covered (Meyer & LeDorz, 2007, Walpersdorf et al., 2010). Indeed, the contrast between geodetic, geologic and geomorphologic slip rate for these faults leads us to think over the mechanism that absorbs the strong NS shear at the northern Lut block boundary. The absence of significant left lateral slip on the two prominent faults indicates that the NS shear accommodation is different from the model proposed by Walker et al. (2004), or that the mechanism changed in time. In this step using complementary geodetic methods like the InSAR technique seems to be necessary to have a better interpretation of these differences between geodetic and short term geologic slip rates. Therefore, the InSAR technique is used in the following to measure the interseismic deformation of these faults.

3 InSAR

Nowadays, Synthetic Aperture Radar interferometery (InSAR) is a common technique for surface deformation measurement because of global coverage, high spatial resolution and remote acquisition possibility (Massonnet et al. 1998, Burgman et al. 2000, Simons et al. 2007). It is used to measure displacements of the Earth's ground due to natural phenomena such as earthquakes, volcanoes, glaciers and landslides. InSAR is based on satellite radar images of the Earth's surface that are obtained by an active remote-sensing method. In a typical space-borne configuration, the radar instrument orbiting at an altitude of 700km emits microwave signals (electromagnetic signal with wavelength that can range from mm to m, 5.6cm in the case of the ENVISAT ASAR instrument) toward the Earth and receives the signals backscattered from the surface. It is an all-weather method as microwave can pass through clouds and is not dependent on solar illumination. SAR uses side-looking radar to illuminate the ground surface along flight direction (figure 3.1).

The SAR image geometry is characterized by azimuth and range direction (Figure 3.1). The azimuth axis is flight direction (along-track), the nadir axis is toward the center of the earth and the range axis is perpendicular to the azimuth (across-track) and nadir axes. These axes define the orbital frame.

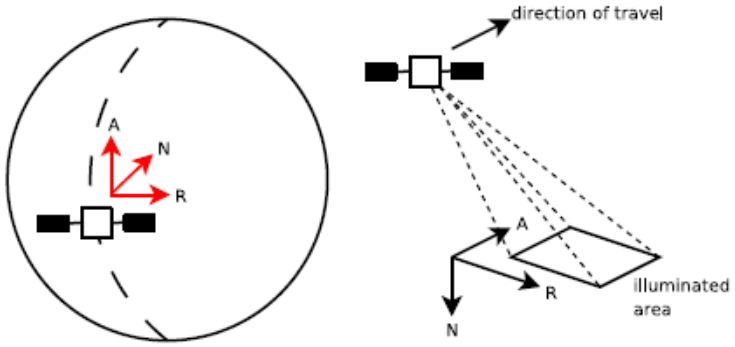

Figure 3.1: Direction of the axes of SAR imagery. Left: Dashed line is the track of the satellite projected onto Earth's surface, A is for azimuth direction that follows the displacement of the satellite, N is for nadir that is the vertical direction from the satellite to the Earth's surface, R is for range that is the range direction corresponding to the looking side direction of the radar (usually on the right). Right: SAR is imaging the area illuminated by its emitted pulse. The line index of a SAR image increases along the azimuth direction and the column index along the range direction (from Peterson Erica H., 2008).

Figure 3.2 represents the geometry of a radar image. The slant range is the distance between sensor and objective in range direction. The look angle is the angle between nadir axis and slant image. The SAR instrument images the surface by emitting successive pulses, each of which illuminates a portion of the ground called footprint (figure 3.2). The rate at which pulses are transmitted and echoes are received is known as the pulse repetition frequency (PRF). The PRF is high enough so that overlapping looks of ground feature are acquired. For the ENVISAT ASAR instrument in image mode, the PRF is about 1650Hz, and a target on the ground is seen by several hundred of pulses. For each pulse, the sampling of the backscattered signal (at 19MHz for ENVISAT ASAR) allows to form one line of the raw image (around 5000 samples for ENVISAT, corresponding to 8m resolution in slant range). The samples are sorted by increasing satellite to ground distance: The first sample corresponds to the Near Range (NR) and is the closest to nadir axis; the last sample corresponds to the Far Range (FR). The swath width is the distance between near and far range.

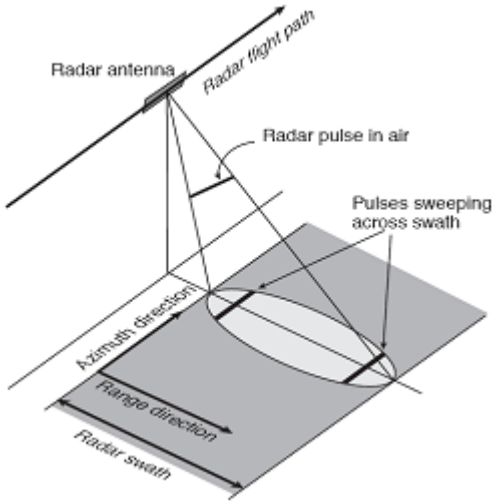

Figure 3.2: Real aperture acquisition geometry and typical imaging scenario for a SAR system. The platform carrying the SAR instrument follows a flight path in azimuth direction. The radar antenna points to the side covering an ellipsoidal footprint in the range direction with one pulse. With multiple pulses emitted and received along the track, the full swath is recorded. From Simons and Rosen (2000)

The resolution of SAR images is different in azimuth and range direction. Range resolution before SAR processing depends on the pulse duration. Azimuth resolution before SAR processing depends on the ratio between signal wavelength and antenna length (see Annex 7.1).

3.1 Phase and amplitude of Radar Image

SAR images consist of complex numbers that correspond to phase (time delay) and amplitude (energy intensity) of the reflected microwave signal from the earth surface. The amplitude of radar image indicates the reflected energy from ground to radar. It is dependant

of the physical and geometrical properties of the ground. The phase for each pixel depends on radar to ground distance, phase delay in the atmosphere, and phase shift due to conjunction of signal at the ground. One pixel contains hundreds of elementary targets, each of them having a different complex reflectivity coefficient thus a different phase shift is obtained by conjunction of signal to them. Therefore the phase image appears as a noisy image with uniformly variable values that are distributed between 0 and 2π (Massonnet & Feigl, 1998). The complex value for each pixel is stored by two real values: the imaginary and real part of the complex. Phase and amplitude can be extracted by the following formula:

$$\varphi = arctg(\frac{I_m}{R_e}) \qquad A = \sqrt{I_m^2 + R_e^2} \qquad (3\text{-}1)$$

Where I_m and R_e are imaginary and real part of complex, respectively.

3.2 SAR Interferometry (InSAR)

The principle of InSAR for measuring ground displacement is to compare the phase of two SAR images of a same area acquired in similar geometrical configuration at two different times. Considering the ideal situation where the atmospheric state and the observed surface properties do not change between the two acquisition dates and where the SAR instrument takes the 2 images exactly from the same point of view, the phase difference between the two images is related to the displacement of the range change (Figure 3.3).However in real situations, such a measurement is made more difficult because the above assumptions are not fulfilled. First of all, the instrument does not exactly take the image from the same position.

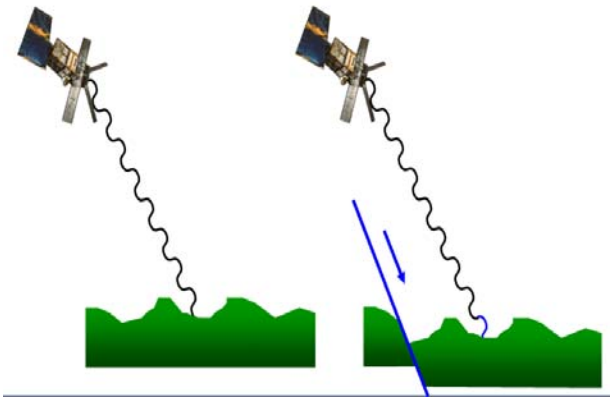

Figure 3.3: As the satellite to ground distance increases between two acquisition date due to surface displacement, the phase measured at each date is also changing. By measuring the phase difference of the two acquisitions, one can have information about the range change.

Figure 3.4 presents InSAR geometry with a different flight path of the satellite. In repeat-path Interferometry, if flight orbits are exactly same in both flights, baseline length will be zero so the phase difference represents pure ground movement; but in reality it never happens. The baseline can be usefully expressed by the perpendicular baseline parameter. In this configuration, there will be changes in phase difference across the image just due to geometrical reasons and even without any surface displacements. For instance, the topography will influence the interferometric phase (i.e. the phase difference between the two images). This effect has to be corrected using a DEM and orbital data to be able to get the surface displacement.

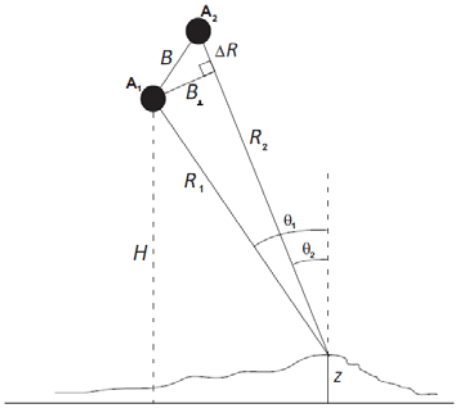

Figure 3.4: InSAR geometry. The satellite is at two different positions at acquisition time A1 and A2; the orbital separation is given by the Baseline B. At acquisition time A1, the distance between a given target on the ground at altitude z and the satellite is R1. The same point (without displacement) is at distance R2 at acquisition time A2. (From Oveisgharan S., 2007)

The range change between ground and satellite is also called Line of Sight (LOS) displacement. If we assume the d vector as deformation on ground, it can be project on LOS by inner product of deformation vector and unit vector in LOS direction. This deformation can convert from radian to cm using the following formula:

$$def_{cm} = \frac{\lambda}{4\pi} def_{rad} \qquad (3\text{-}2)$$

3.3 Applications and limitations

Synthetic Aperture Radar (SAR) is a remote-sensing technique that acquires data at daylight or night and without weather limitation. It is a technique for extracting three-dimensional information of the earth's surface with high spatial sampling close to 10 m on ground, high resolution close to mm-cm using InSAR processing. This technique also has a temporal resolution of 35 days to take the next image from a specific area.

The figure 3.5 from Massonnet & Feigl, (1998) presents the field of application of INSAR taking into account five parameters: The pixel size, the swath width, the upper and lower

limits of the amount of deformation gradient, and the phase and atmospheric noise levels. Detectability depends on the event's magnitude and spatial scale. They make a truncated parallelogram in the width of a deformation signal versus the amount of range change. An interferogram cannot distinguish deformation beyond these gradational boundaries. Some of them like pixel size and swath width bounds are physical limitations that depend on the spatial wavelength of the deformation signal. Deformation signals with spatial wavelengths smaller than an image pixel or much larger than the size of an image scene cannot be detected with InSAR alone. Atmospheric noise and phase noise levels influence the smallest displacement signal in any spatial wavelength (Perice J. E., 1999).

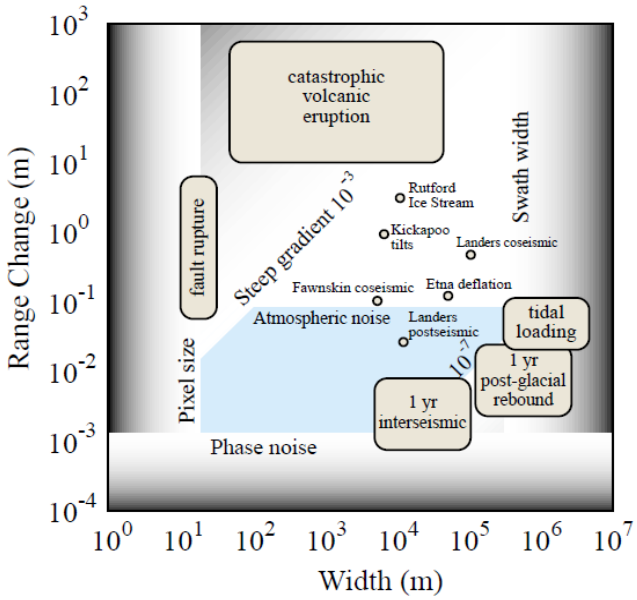

Figure 3.5: classification of crustal deformation signals by width and range. Massonnet & Feigl, 1998(from Perice J. E., 1999)

Wright et al. (2001) determined Interseismic strain accommodate across the North Anatolian Fault using InSAR techniques They processed 12 pairs image across the fault with geodetic slip rate 24±1mm/yr with temporal separations between 1.2 and 3.8 years, the slip rate on the fault was determined by minimizing the misfit between dislocation model and observed phase profile and find it equal to 22mm/yr. Cavalié et al. (2008) used interferometric synthetic aperture radar data from 1993 to 1998 with baseline smaller than 200m that cross the Haiyuan fault, part of a major left-lateral faults system at the northern edge of the Tibet-Qinghai plateau, the derived slip rate 4.2-8mm/yr that consist with GPS slip rate. Finally Wright et al. (2004) used 500-lm long strips of radar data acquired by ERS-1 and ERS-2 satellites between 1992 and 1999 to observe low slip rate on the major faults of the western Tibetan plateau and after staking 5 images and right-lateral slip rate of the Karakoram fault was found to be in the range of 1±3mm/yr. This situation is close to our case study, so we expect to derive interseismic deformation for these low slip rate faults.

4 Interseismic deformation measurement by InSAR

In this part, we investigate how SAR interferometry technique can contribute to the measurement of interseismic deformation across the Doruneh and Dasht-e-Bayaz faults. After a presentation of the dataset used in this study, the data processing from the raw data to the construction of profile of ground displacement rate across the fault is explained. Then a comparison of the results with an analytical model of interseismic displacement is performed

4.1 InSAR data

Synthetic Aperture Radar (SAR) images from the ASAR instrument (wavelength of 5.6 cm) on board the ENVISAT satellite have been used in this study to investigate interseismic deformation across the Doruneh and Dasht-e-Bayaz faults. In the “image mode” of the ASAR instrument (swath of 100km), the studied area is covered by several tracks of the satellite, amongst which two tracks have been particularly studied in our work (track 392 and track 435, see location in Figure 4.1).

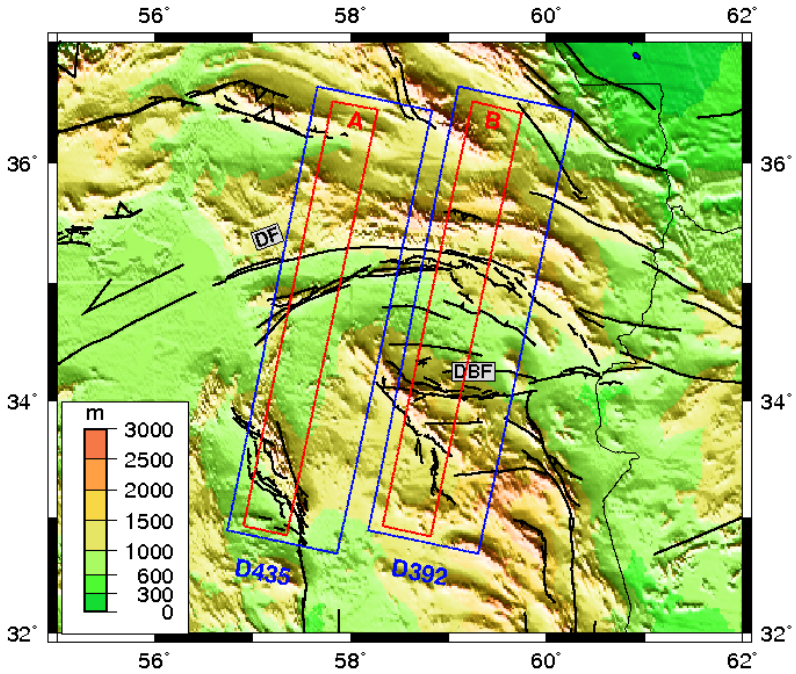

Figure 4.1: Coverage of ENVISAT images acquired on two different descending tracks (blue boxes). Background is a shaded DEM (SRTM), black lines indicate active fault traces (DF: Doruneh Fault, DBF: Dasht-e-Bayaz Fault). The two green boxes give the location of two profiles discussed in the following sections. Scale bar shows the altitude of region that is in ranges 600 to 1500 m.

On each of the track about 24 images, corresponding to different dates of acquisition, have been ordered at the European Space Agency (ESA). This has been done through an ESA Cat-1 project (n°7023, Principal Investigator: Zahra Mousavi). These images were acquired in descending orbit (i.e. satellite flying from North to South) from 2003 to 2010. Some of them were archived images but we also requested new acquisitions in 2010 for our project. The perpendicular baseline distributions of the available images through time for track 392 are given in Figure 4.2. The perpendicular baseline difference between two images is an important parameter in InSAR: a small baseline means that the two images were taken from a close point of view, which optimizes the quality of the INSAR signal. We selected images within a limited baseline range (blue area in Figure 4.2). To start our study, we processed amongst these images only image pairs having a time difference larger than 1 year (to maximize the interseismic tectonic signal that built up with time) and baseline differences less than 100-150m to minimize the signal decorrelation. The maximum and minimum time intervals between selected images are 6.75 and 1.08 years. A similar selection has been done for track 435.

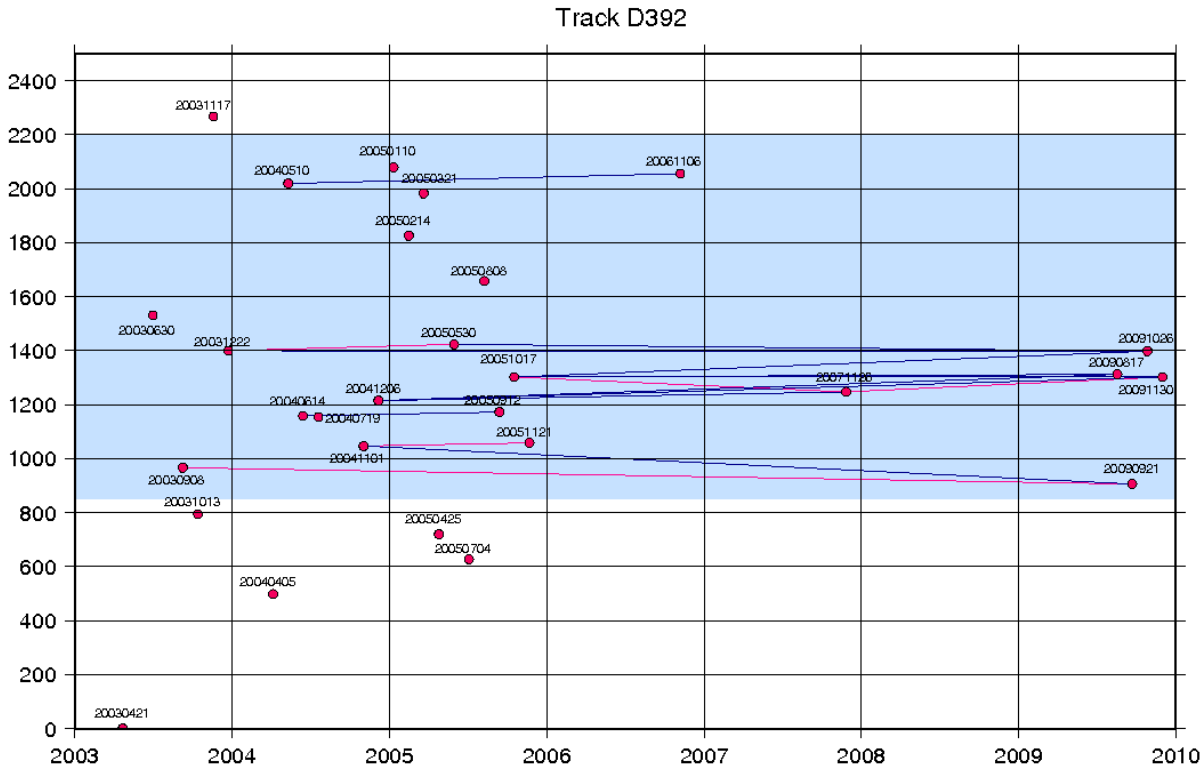

Figure 4.2: Example of baseline distribution through time for ENVISAT SAR images acquired along track n°392. The blue area shows the range of baseline used to select the images. The lines linking pair of SAR images show the interferograms used in this study. The dark blue lines correspond to interferograms used in the final results and the pink lines correspond to interferograms that have been discarded because they are affected by important atmospheric perturbation implying a high correlation between phase and topography masking the tectonic signal (see section 4.2).

4.2 Image processing

The raw radar images (Processing Level 0) were processed with ROI_PAC (Repeat Orbit Interferometry PACkage) which is a JPL/Caltech software for processing InSAR data (Rosen et al. 2004) (see annex 7.2). The topographic phase contribution was estimated from the SRTM Digital Elevation Model (DEM) at 90m spatial resolution (Farr et al. 2007). Precise DORIS orbital data for ENVISAT satellite provided by ESA are used for interferometric processing. In the following, we present results based on 16 interferograms of track 392 that were used to investigate the deformation signal related to the Doruneh and Dasht-e-Bayaz faults. First of all, we show examples of individual interferogram illustrating some of the difficulties making the interpretation of the phase variation of a single interferogram as a displacement map impossible for small interseismic gradient of displacement (less than 1cm over 100km, translating into 2.2 radians phase change across the interferogram). In the case of North-Eastern Iran, a first source of noise comes from the fact that part of the studied area is covered by sand dunes. As these sandy areas are changing rapidly through time, the spatial coherence of the interferometric phase is very low in interferograms spanning several years. It is then impossible to unwrap the phase for the whole interferogram.

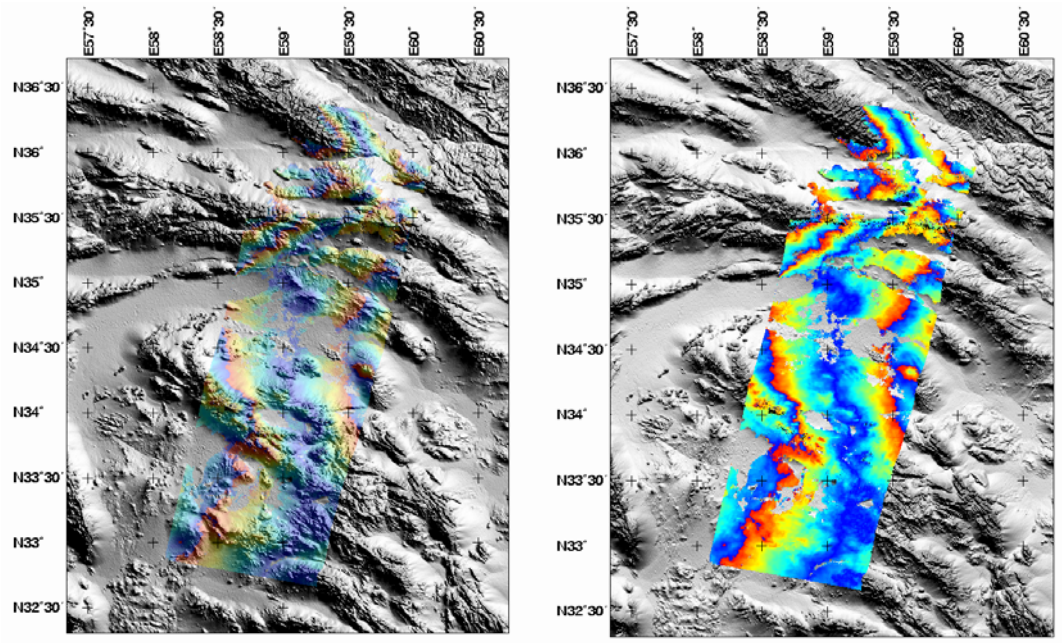

Figure 4.3: Background is a shaded DEM where the largest flat areas (homogenous light grey) correspond to sandy desert. In color, the unwrapped parts of the interferogram 2005-10-17-2007-11-26 (2 years) are shown with transparency on the left and without transparency on the right figure (one cycle of color corresponds to 2 pi radians phase change). Note that areas that have not been unwrapped are related to the sandy areas. In this example the curved North-South fringes (approximately parallel to the flight path) are related to unmodeled orbital errors (clearer on the right image) showing an E-W phase gradient. The small scale (10km) variations of the fringe pattern (blobs) in Fig. 4-4 are due to atmospheric perturbations. Orbital error and atmospheric signal dominates the expected tectonic signal.

Figure 4.3 presents this unwrapping problem, illustrating the difficulty when analyzing the Doruneh fault because, in this track 392, the fault is located right at the boundary between sandy and mountainous area. Phase variations in some interferograms can also be dominated by long wavelength phase ramps due to unmodeled orbital errors (figure 4.3-left) in the flattening step (see Annex): a small amount of phase gradients due to orbital errors of the flight path remains. Figure 4.4 illustrates another source of noise related to atmospheric perturbations in interferogram: the interferometric phase can be correlated to topography, which is due to a change of the stratified atmosphere between the two acquisition dates. These perturbations make the detection and the interpretation of the tectonic signal more difficult.

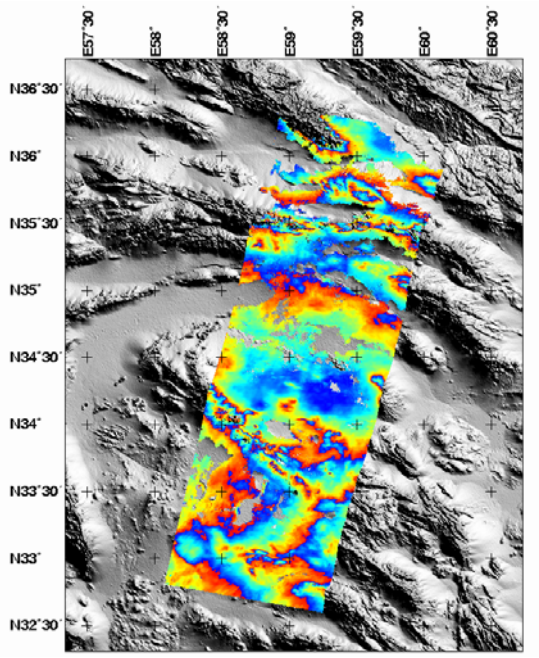

Figure 4.4: Interferogram between dates 20040614and 20050912 showing fringes correlated to the topography and irregular blobs due to atmospheric change between the two acquisition dates (one cycle of color corresponds to 2 pi radians phase change that, if interpreted as ground displacement, would correspond to 2.8 cm of displacement along the radar line of sight). Background corresponds to a shaded DEM.

Although atmospheric and orbital errors are perturbing the tectonics phase signal, if a shallow creep on a fault is present, it could be detected in such interferograms as it will result in a sharp phase variation located exactly along the fault trace. We performed a close visual examination of the interferograms and the active faults map looking for such signal, however no evidence of creep has been found along the identified active fault covered by our interferogram, indicating that there is probably no superficial creep exceeding 1mm/year.

To further investigate the long wavelength tectonic signal due to interseismic strain accumulation, we follow the stacking approach from Wright et al. (2001). In this approach, independent unwrapped interferograms are stacked together on a pixel basis. The sum of the unwrapped phases is divided by sum of the interferogram duration times. If we assume

that the fault is in steady state, the stack indicates the mean interseismic velocity field of the fault. In averaging independent interferograms covering long time span, the tectonic deformation signal will be enhanced with respect to atmospheric and orbital errors to, assuming that orbital errors and atmospheric perturbations, which are not correlated with time, will cancel out (Zebker et al., 1997). Figure 4.5 show a stack of all the 16 computed interferograms (see figure 4.2) and the time counting of the stack. Time counting is done pixel by pixel by summing the interval times of interferograms

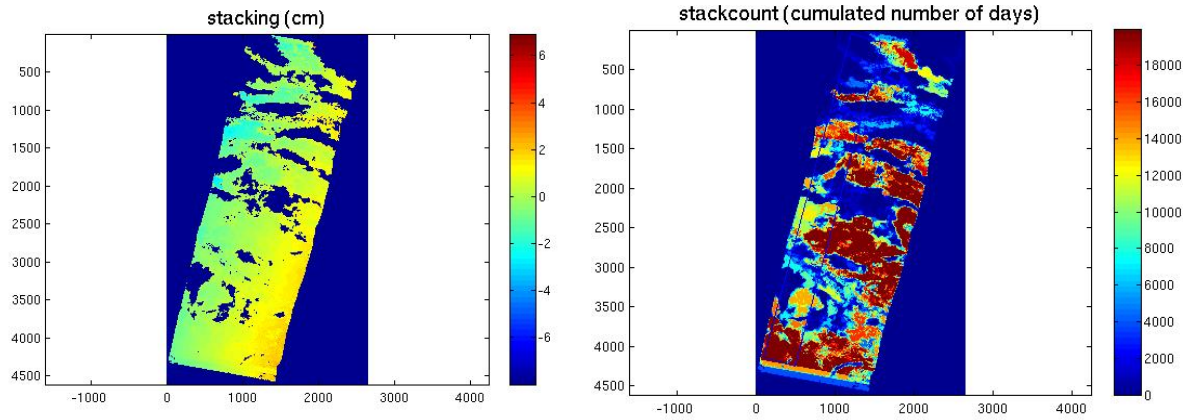

Figure 4.5 :Left: Stack of 16 unwrapped interferograms for track 392 . Positive values indicate an increase of the range toward the satellite. The time span covered is from 2003 to 2009. In the right, time counting is given. Note that in some part due to unwrapping problem in sandy area, the time cover of the unwrapped data is less.

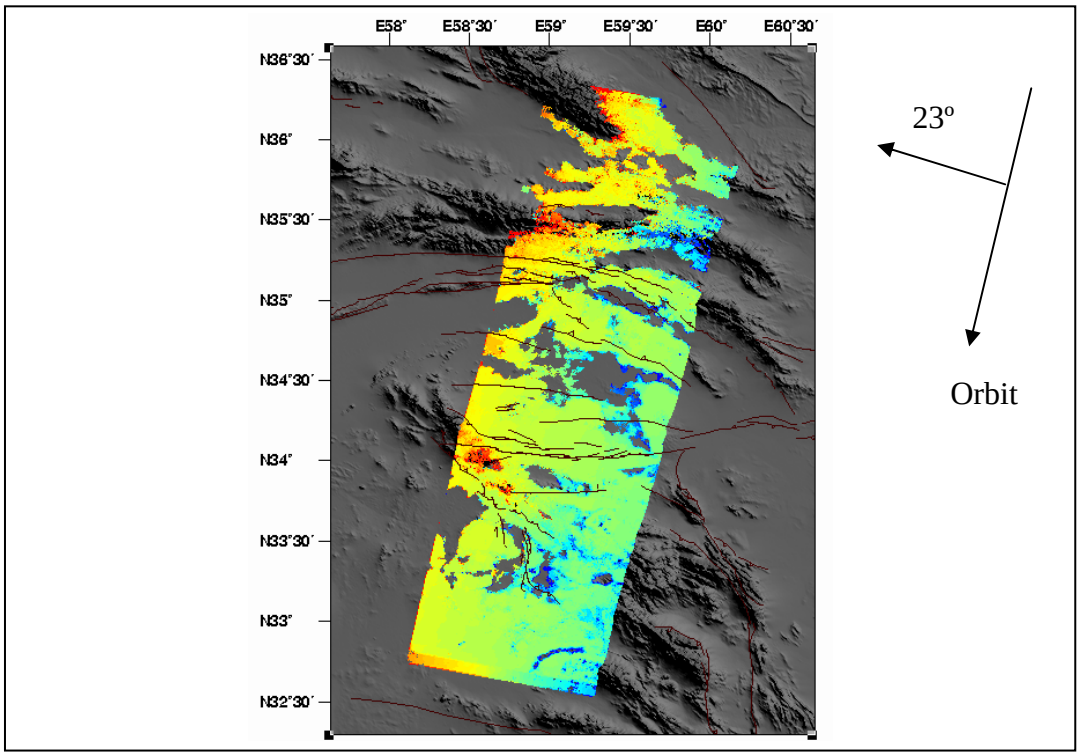

Figure 4.6: Average velocity map (cm/year) for track 392. The color scale starts from -2.41 cm (blue) to 1.91 cm (red). Phase increase between 2 points A and B, means point B is going toward the satellite with respect to A. We convert radian convert radian into distance along Line of Sight. . The blue rectangle indicates the box along which the cumulated profiles in Fig. 4-7 have been calculated. We keep the pixel with minimum interval time 1000 days.

. Figure 4.6 presents the velocity field that is obtained by dividing the cumulated range difference by the time count of the interferograms pixel by pixel. The InSAR phase change is converted to the variation along line of sight (see part 3.)

In the stack of all the interferograms (fig 4.5), a significant East-West gradient is visible which is far larger than the expected tectonic signal and not in the expected direction. An examination of the individual interferograms of the stack indicates that it corresponds to remaining orbital errors that do not cancel out enough in this stacking approach. Furthermore, local variations are also present that can be attributed to (1) atmospheric perturbation not removed by the stacking approach, (2) unwrapping error, (3) heterogeneity of the time count used. As the expected tectonic signal is a North-South ground displacement gradient across the fault, to enhance the deformation signal with respect to the local variations, an North-South averaged profile is created along track (perpendicular to the Doruneh fault, see Figure 4.6). This profile is 300km long and 54km wide and crosses both the Doruneh and Dasht-e-Bayaz faults. A weighted averaging (the weight of each point is given by the cumulated time from stack counting) along the profiles is done for bins of 1800m length computed every 900m (see figure 4.7).

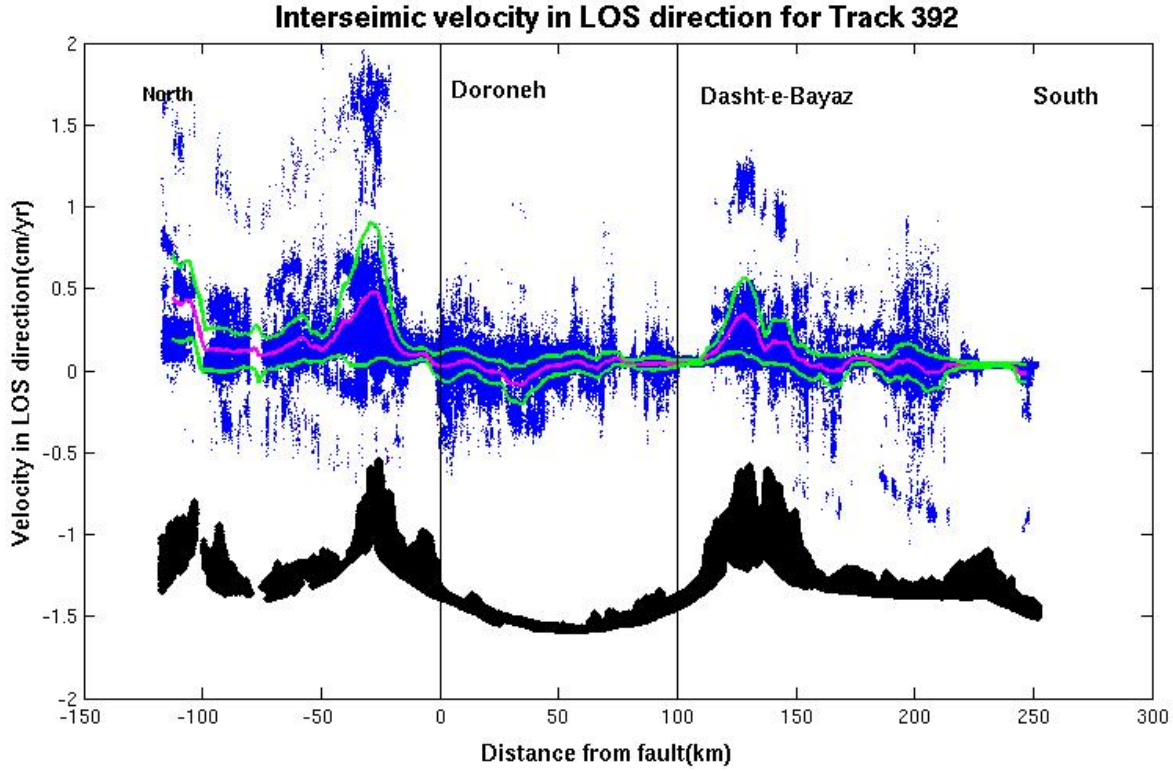

Figure 4.7: Cumulated profiles (see box location in fig 4.6). Each blue dot represents a pixel of the stack of interferograms located within the box. Distances are given with respect to the Doruneh fault. The pink line represents the weighted averaged profile (using a moving average window with a size of 1.8km). The green lines represent one standard deviation bounds. The black dots represent the topography pattern along the same profile. Note the jump in the InSAR velocity field at -40km that is related to unwrapping errors.

The resulting profile shows a North to South decreasing trend. However this trend is difficult to interpret because it could be related to orbital error as mentioned herebefore. This first profile is including all the interferograms without correction and then including orbital errors, unwrapping errors and also atmospheric errors a part of which are correlated to the topography. To better estimate the need to correct from these errors or to exclude the noisiest interferogram it is necessary to look at the individual interferogram profiles. Figure 4.8 shows the individual averaged profiles for each interferograms used in the stack. To create an individual velocity profile, at first the range difference along the profile is divided by the time span of the corresponding interferogram.. For better comparing the velocity profiles, one can remove the linear long wavelength trend of each plot (this is done by a least square method). Figure 4.8-right presents the detrended LOS velocity. But still, it is hard to compare the velocity because the profile must have a same reference point. Interferograms are only giving relative information between pixels and can therefore be adjusted by adding a constant. Figure 4.9 shows the detrended profiles with a common reference point located at the Doruneh fault.

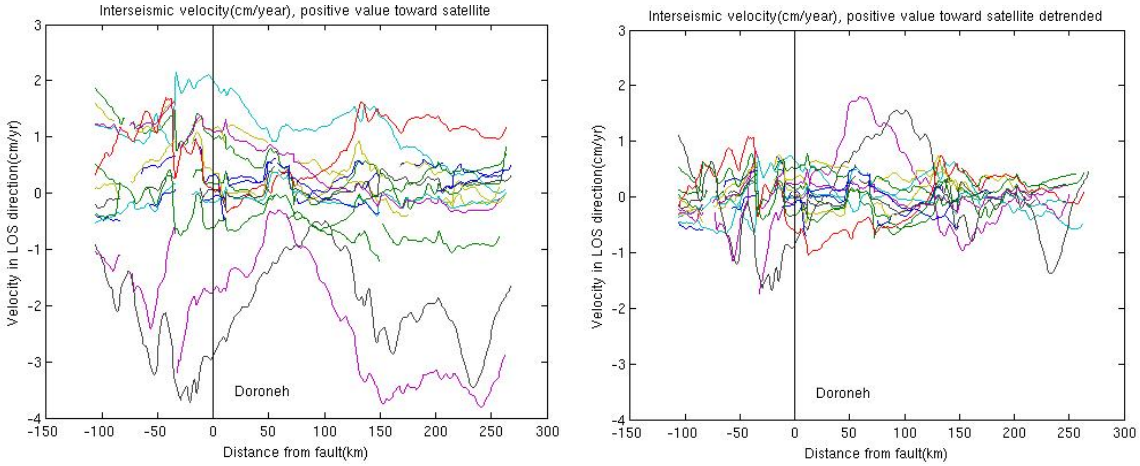

Figure 4.8: On the left, profiles along track that are obtained by dividing the range difference by the time span covered by each interferogram. On the right, the linear trends of the profiles are removed by a least square method. Positive values in the profiles indicate an increasing range toward the satellite. The horizontal axes present the distance from the fault.

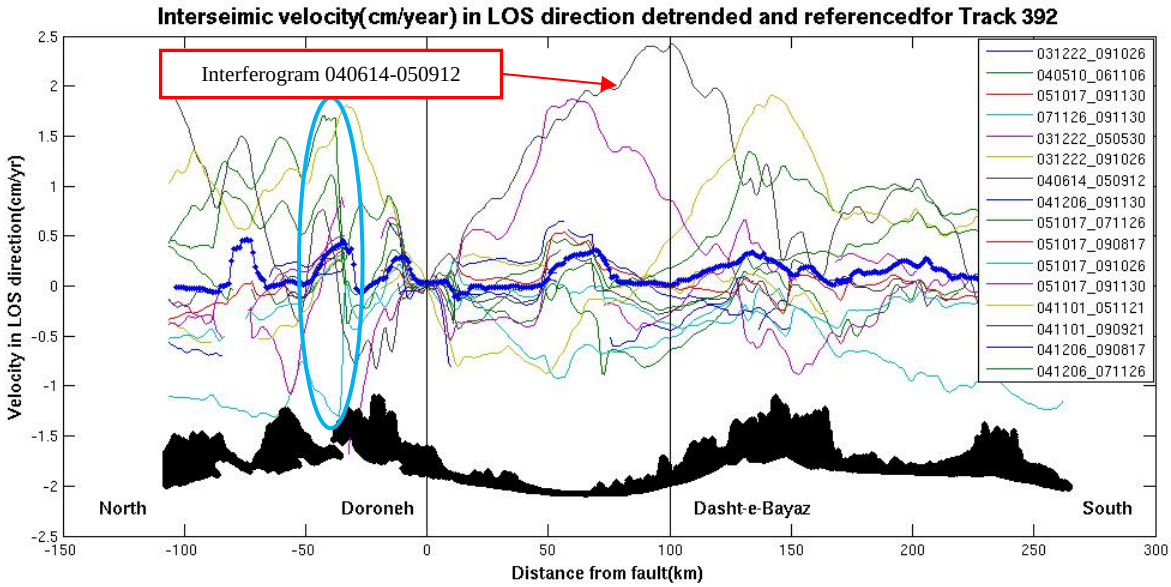

Figure 4.9: The interseismic velocity in LOS direction along profiles of individual interferograms after detrending and adjustment around the Doroneh fault as reference point. The black curve indicates topography along the profile. It is clear that some of the interferograms are correlated to topography. The ellipse shows a phase jump affecting interferogram 051017-091130 corresponding to the unwrapped error in some of the interferograms due to sandy area.

Figure 4.9 shows large variations amongst the profiles. These variations are not correlated with the time covered by the interferograms. Based on a visual inspection, nterferograms which have clear huge perturbations, correlation or anticorrelation with topography (Figure 4.9), which is due to atmospheric effect are removed to improve the quality of the stack. For instance, the 040614_050912 interferogram show a clear correlation between phase and topography as illustrated in figure 4.10. .

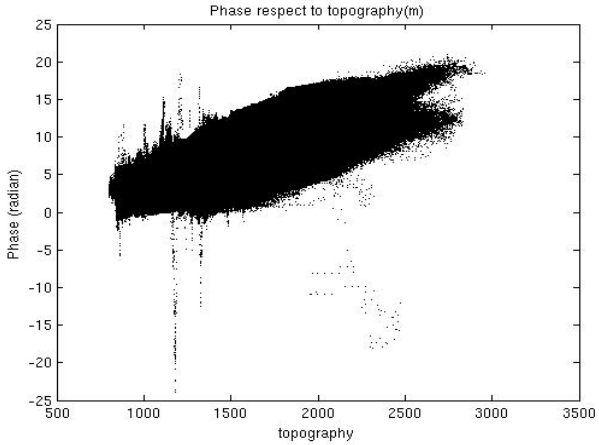

Figure 4.10: Correlation between phase and topography for interferogram 040614_050912. A clear nearly linear relationship between phase and topography appears for this interferogram. is clear for. The vertical axis is the unwrapped interferometric phase in radian.

4.3 Interseismic velocity model

To interpret the InSAR observations it is helpful to quantify the expected pattern of interseismic deformation for the given fault configuration. InSAR measures the component of deformation in the satellite line of sight, which is 23º from vertical at the swath center and perpendicular to the satellite flight direction. Thus, the interferograms are most sensitive to horizontal motion in a direction N78º W (Wright et al., 2001). These two left-lateral faults are roughly parallel to this direction (figure 4.11).

Savage and Burford (1973) introduced a dislocation model for the strike-slip fault. They assumed that slip on the fault is zero down to the locking depth *d* but it is an amount of *b* below depth *d* (in other words the fault is freely slipping below the locking depth):

$$v = \frac{b}{\pi}\arctan(\frac{x}{d}) \qquad (4\text{-}1)$$

Where *x* is distance from fault.

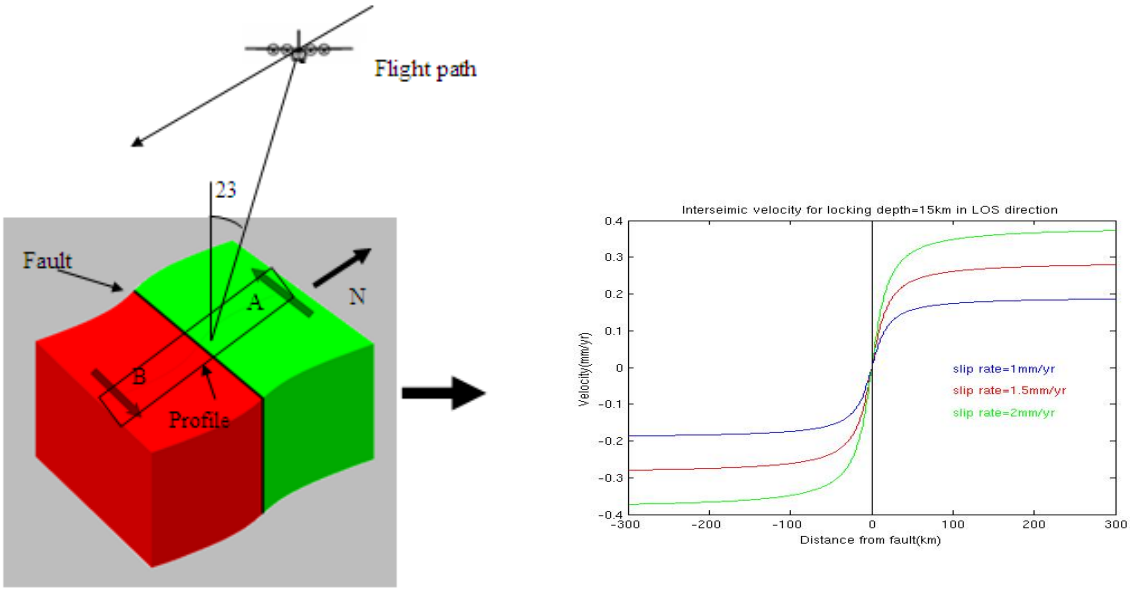

Figure 4.11: On the left, a scheme relating LOS displacement and fault orientation for a left-lateral strike-slip fault. According to the fault orientation with respect to LOS, the northern block is moving away from the flight path and the southern block is moving toward the flight path. On the right, expected displacement rates according to the elastic dislocation model for a left-lateral fault with a locking depth equal to 15km depth. The theoretical displacement rates in LOS direction are obtained for horizontal fault slip rates equal to 1, 2 and 3 mm/yr.

According to this model, assuming a locking depth of 15 km (this locking depth is approximately consist with the depth of seismicity in the east of Iran), and taking into account the radar viewing geometry (azimuth N78°W, and incidence angle of 23°), we can calculate the expected displacement rate along LOS for points on a cross section across the fault (Figure 4.11-right).The fault geometry used is a straight vertical fault striking E-W for track

392., Different far field fault slip rates are represented, a slip rate of 2 mm/yr yielding a total LOS displacement rate of 0.8 mm/yr at distances of more than 100 km from the fault. Figure 4.12-left indicates that for a left-lateral fault oriented roughly EW, point A in the northern block moves away from the satellite and point B in the southern block moves toward the satellite. The velocity in horizontal direction can convert to LOS direction by formula 4-2; thus 1 cm/yr deformation in LOS is 2.64mm/yr on horizontal.

$$v_{LOS} = v(\sin 23^\circ \times \cos(90 - 78^\circ)) \qquad (4\text{-}2)$$

If we assume the simplest condition that the whole regional deformation is related to the activity of the Doruneh fault, and in particular that no earthquake occurred on this fault in the last years, we can suppose that the phase variation in our interferograms is reflecting the interseismic deformation across the Doruneh fault. The phase variation in LOS direction for individual interferograms the expected tectonic signal.are given in figure 4.12 after removing the 4 noisy interferograms mentioned before.

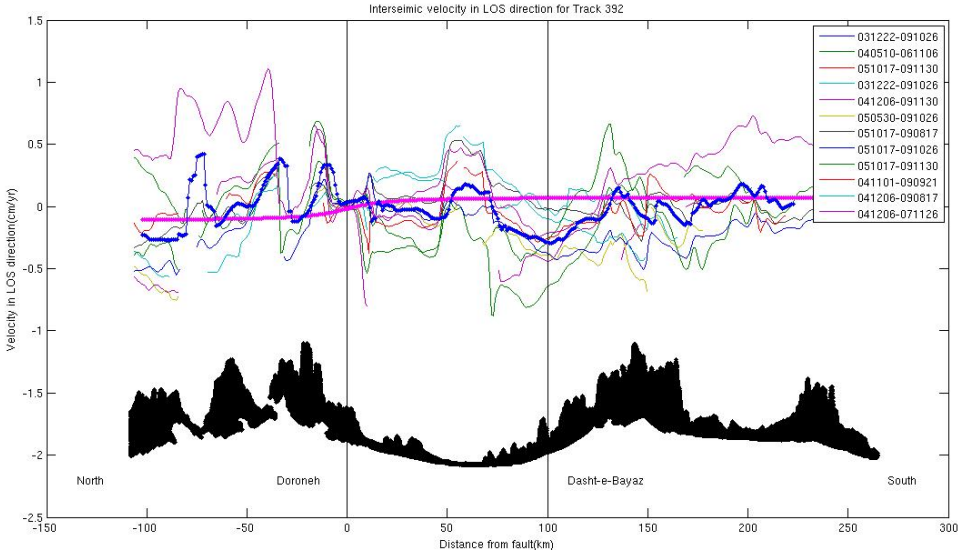

Figure 4.12: The weighted average of individual interferograms in each bin with 1800m length (bold blue line) with topography (black dot). Note the location of Doroneh and Dasht-e-Bayaz fault, with the velocity profiles centered on Doruneh. We plot a dislocation model with respect to this fault with 30km locking depth and a total horizontal slip rate equal to 5 mm/yr (bold pink line). The data do not constrain any arctangent shape, not even for 5mm/yr slip rate, due to the low signal to noise ratio.

Note the large differences between the individual InSAR velocity profiles that are related to unwrapping errors and tropospheric artifacts correlated to topography. Even when calculating the average velocity profile, like for the stacking results, it is hard to find the deformation signal. We try to compare the velocity model for a slip rate of 1mm/yr (geodetic slip rate) and 2.4 mm/yr (geomorphological slip rate) with the InSAR data, but unfortunately the perturbation of the interferometric signal is too high to constrain such small slip rates. To

illustrate this problem, we superpose an interseismic model with a slip rate of 5mm/yr atop the velocity profiles that should overestimate the expected slip rate to show that the InSAR results are not yet capable to estimate horizontal slip rates below 5 mm/yr. The comparison of the profiles with the model does not show a tectonic signal similar to the expected simple interseismic model. Then we processed 22images of track nº435 and more images for track nº392 (25 images). It seems in figure 4.12 profile A for track 435, the noise decrease in relative to figure 4.12 just by increasing the number of images, so if we increase the time span, the result will be more precise.

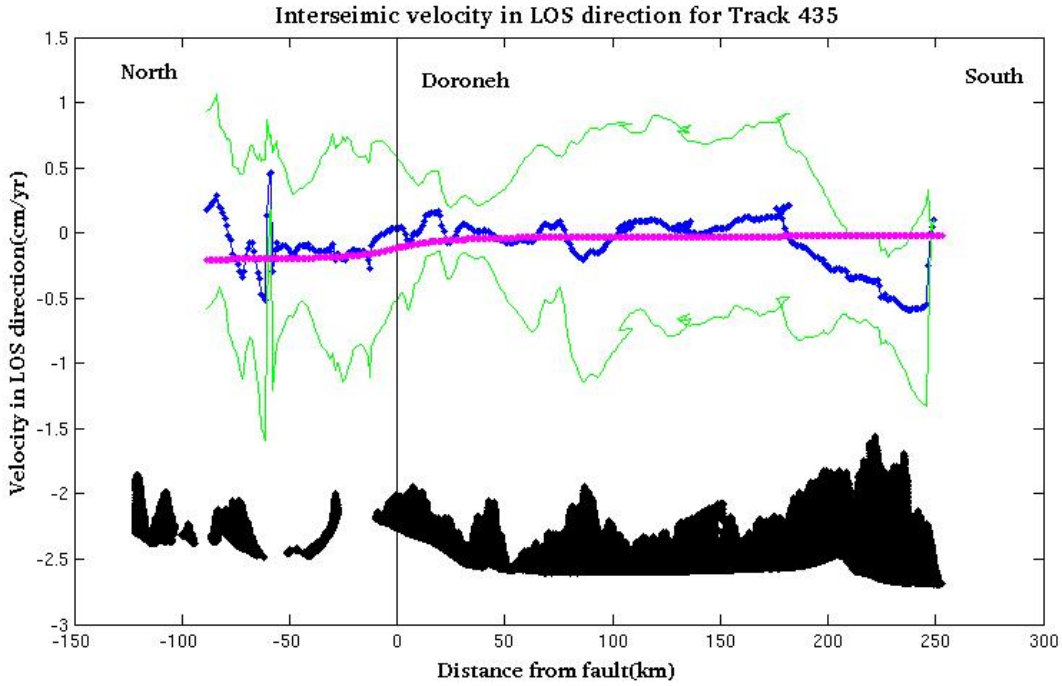

Figure 4.13: The weighted average of individual interferograms in each bin with 1800m length (bold blue line) with topography (black dot) for track 435 profile. Note the location of Doroneh fault, with the velocity profiles centered on Doruneh. We plot a dislocation model with respect to this fault with 30km locking depth and a total horizontal slip rate equal to 5 mm/yr (bold pink line). In interseismic model we assume that Track 435 only cross Doruneh fault.

5 Discussion and conclusion

We processed four tracks of ENVISAT images. We focused on track n°392 (16 interferograms) track n°435 (22 interferograms). A stack of interferograms has been established in order to enhance the deformation signal and mitigate the turbulent part of the atmospheric perturbation. However, the stack results still present high correlation between phase variation and topography due to the stratified part of the atmospheric perturbations. Visual inspection of individual interferograms allows us to identify 4 interferograms showing a clear high phase-topography correlation. After removing these interferograms, the signal to noise ratio of the profile stack is still too high to be able to identify a clear tectonic signal. A dislocation model from Savage and Burford (1973) was used to help to distinguish interseismic deformation. According to this model, we expected to have a tangent shape displacement rate profile along track with the northern block moving away from the satellite (increasing LOS) and the southern block moving toward the satellite (decreasing LOS). However the InSAR signal does not show any evidence of a pattern similar to the one expected from the elastic dislocation model. Once the noise level sufficiently reduced, we can use InSAR for deriving faults slip rates, assuming that the normal component of the fault displacement is negligible. To interpret the InSAR results, theoretical slip rate estimations will be computed based on the dislocation.

One can argue that on track 392 the deformation is distributed on several other faults, As for instance according to the rigid block model and the block dimensions of tectonic model, 10 mm/yr cumulated over both the Doruneh and the Dasht-e-Bayaz faults (Walker et al. (2004). That means, somewhere between 10 for Doruneh and 0 for Dasht-e-Bayaz, and 0 for Doruneh and 10 for Dasht-e-Bayaz is accommodate on these faults..

The track 435 has the advantage to not include the Dashte-Bayaz fault (even if other Nyband fault with geodetic slip rate *of 1-2 ± 1 mm/yr* to the South exist). we processed more images for track 435 that cross middle part of Doruneh, The average profile may present an arc tangent shape similar to the model but again the signal to noise ratio is too low to conclude. .

Consequently, one can ask the question if the tectonic signal is too small to be measured by INSAR technique. According to section 3.3, to be detectable with InSAR techniques, the tectonic signal has to fulfill several criteria. These main criteria are related to the pixel size, the swath width, the upper and lower limits of the deformation gradient measurable by InSAR (see figure 3.5). For this study, the critical criteria are the lower limit of the measurable phase gradient because of atmospheric effect and orbital error. According to the model, one can

expect a deformation of 10^{-8} for one year that is a few millimeters distributed over hundreds of kilometers per year. As 7 year of data is available, one can expect deformation of 10^{-7} which is the order of magnitude of the lowest gradient detection achievable by the ASAR instrument on board ENVISAT (Massonnet et al. 1998). Precedent study have measured interseismic deformation using InSAR technique for the North Anatolian Fault, the Haiyuan fault and Karakorum fault with slip rates of 24±1mm/yr, 4.2-8mm/yr and 1±3mm/yr, respectively (Wright et al., 2001 , Cavalié et al., 2008 and Wright et al., 2004).

Further data will be available up to October 2010 (about 5 more dates per track), that will make possible to produced more independent interferograms with slightly more tectonics signal compared to our study and consequently increase the signal to noise ratio. However, the improvement needed seems to be above that: our work has shown that a simple stacking approach is not enough to achieve our goal. Thus, it seems necessary to improve the InSAR analysis method applied in this study. Several paths can be followed: an improvement of the signal to noise ration can be obtained by using all the possible interferograms instead of a selection of them following the so called “Small Baseline” strategy and using the overlap area between tracks that increase signal to noise ratio. This approach allows a better detection of unwrapping errors, a more consistent orbital correction and a correction of the interferogram from the phase-topography correlation. Another strategy could be to mitigate the atmospheric perturbation which seems to be the most important source of error by using of GPS measurements of the tropospheric delay to correct the interferograms. The availability of a permanent GPS network in the area makes this approach feasible. A first test of the feasibility of this approach has been done using Zenith Total Delay (ZTD) value provided by the Iranian permanent GPS network (IPGN). In order to find whether it is possible to mitigate the tropospheric error using GPS observation, an interferogram with a short interval time span (2months) has been processed with ROI_PAC and compare to the simulated interferogram based on interpolated ZTD value converted into interferometric phase (Figure 5.1). The first result are encouraging, however the ZTD value are not available before 2007, which limits the number of interferogram that may benefit from this correction. Alternatively, global meteorological models like ERA-Interim could be used to reduce this major error source in the interferograms (e.g. Doin et al, 2009).

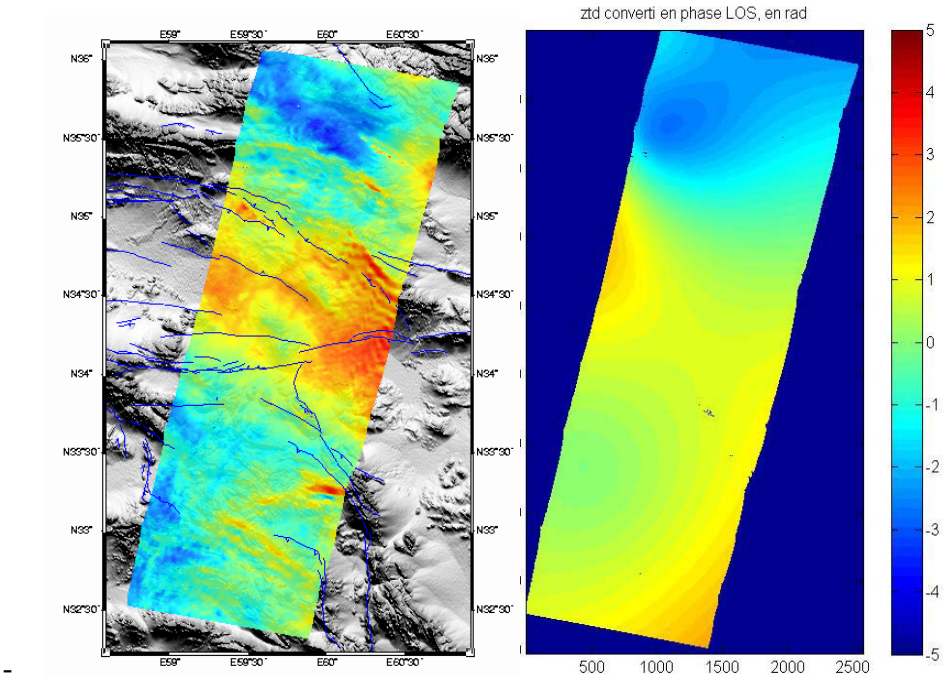

Figure 5.1: Left: interferogram 070829-071107 with only 2 months interval in which the phase signal can be assumed to be only due to atmospheric effects and orbital errors. , Right: with the same color scale, the interferometric phase modeled from Zenital Total Delay (ZTD) estimation from permanent GPS stations and interpolated. Note the relatively good agreement between the two images meanings that ZTD value could be used to mitigate long wavelength atmospheric effects. (Only a few GPS stations are constraining the interpolation, that's why they cannot reproduce the short wavelength phase variation of the interferograms).

5.1 CONCLUSION

In this study, we concentrated on two EW oriented target faults in the east of Iran, on the northern boundary of the aseismic Lut block. We wanted to answer open tectonic questions concerning these two major faults, the Doruneh and the Dasht-e-Bayaz fault. The contrast between interseismic slip rates measured by GPS (<1 mm/yr) and geology (2.5 mm/yr for both faults) motivated us to improved the spatial resolution of these sparse measurements. Is there local aseismic creeping phenomena accommodating part of the deformation or is the deformation distributed at long wavelength according to classical interseismic model on strike-slip faults. The InSAR method has been chosen for its potential to answer such question, however considering the expected low gradient of the tectonic signal, we are clearly at the limit of the method. As individual interferograms are useless to give such measurement, we choose to first test the simplest approach to enhance the tectonic signal that is the stacking approach applied successfully on other strike-slip fault. A first result of our work is that there is no significant superficial creep (i.e. > 1mm/yr) on the Doruneh and Dasht-e-Bayaz Fault during the examined period 2003-2007. A second result is that the

stacking approach does not allow detecting the tectonic signal because of the remaining orbital error and atmospheric effects in the results. This open perspective of improvement of the methodology that will also benefit from further data acquisition up to October 2010. For instance the use of the more sophisticated technique as SBAS combined with different atmospheric correction strategies, could really allow us to give useful constraints on the expected weak tectonic signal.

6 Bibliography

Ambraseys, N. N., and C. P. Melville, 1982. A History of Persian Earthquakes, CambridgeUniv. Press, New York.

Bamler R. , 2000, Principles pf Synthetic Aperture Radar, Survey in Geophysics ,21, 147-157

Berberian, M. & Yeats, R., 1999. Patterns of historical earthquake rupture in the Iranian Plateau, Bull. Seism. Soc. Am., 89, 120–139.

Bechor, N. 2006; Extending interferometric synthetic aperture radar measurements from one to two dimensions, PhD Thesis, STANFORD UNIVERSITY

Cavalié et al, Measurement of interseismic strain across the Haiyuan fault (Gansu, China), by InSAR, Earth and Planetary Science Letters 275 (2008) 246-257.

Doin, M. P., C. Lasserre, G. Peltzer, O. Cavalie, and C. Doubre (2009), Corrections of stratified tropospheric delays in SAR interferometry : Validation with global atmospheric models, J. Appl. Geophys., v. 69(1), pp. 35-50, doi : 10.1016/j.jappgeo.2009.03.010.

Emardson T. R., Simons M., Webb F. H., 2003; Neutral atmospheric delay in interferometric synthetic aperture radar applications: Statistical description and mitigation, Journal of Geophysical Research, Vol. 108, No. B5, 2231

Farr, T. G., et al. (2007), The Shuttle Radar Topography Mission, Rev. Geophys., 45, RG2004, doi:10.1029/2005RG000183.

Fattahi, M., Walker R. T., Khatib M. M., Dolati A. & A. Bahroudi, 2006, Slip-rate estimate and past earthquakes on the Dorouneh fault, eastern Iran, Geophys. J. Int. 168**,** 691–709

Fielding, E. J., Lundgren, P. R., Bergmann, R. and Gareth J. Funning, (2009), Shallow fault-zone dilatancy recovery after the 2003 Bam earthquake in Iran, Nature 458, 64-68 doi:10.1038/nature07817.

Funning, G. J.; Parsons, B.; Wright, T. J.; Jackson, J. A.; Fielding, E. J. (2005), Surface displacements and source parameters of the 2003 Bam (Iran) earthquake from Envisat advanced synthetic aperture radar imagery. J. Geophys. Res., Vol. 110, No. B9, B09406 http://dx.doi.org/10.1029/2004JB003338. Gareth J. Funninga, Richard M.D. Barkea, Simon H. Lamba, Estela Minayab, Barry Parsonsa, Tim J. WrightaThe 1998 Aiquile, Bolivia earthquake: A seismically active fault revealed with InSAR

Ghiglia D. C. and M. D. Pritt, 1998; Two dimensional phase unwrapping: theory, algorithm and software, John Wiley and Sons

Hooper A, Segall P.,Zebker H., 2007, Persistent Scatterer InSAR for Crustal Deformation Analysis, with Application to Volc_an Alcedo, Gal_apagos, JOURNAL OF GEOPHYSICAL RESEARCH,

Hooper, A., A multi-temporal InSAR method incorporating both persistent scatterer and small baseline approaches, Geophys. Res. Letters, doi:10.1029/2008GL034654 (2008).

Jackson, J.& McKenzie,D., 1984. Active tectonics of the Alpine-Himalayan Belt betweenwestern Turkey and Pakistan, Geophys. J. R. astr. Soc., 77(1), 185–264

Jadidi Mardkheh A., 2007, Analysis of the Iranian Permanent GPS Network in the NE and E of Iran (time series and velocity field) and Modeling the stress transfer between active faults bounding the Lut block", Master thesis LGIT, UJF 2008.

Li Z. & Bathel J., 2008, Image coregistration in SAR Interferometry, The International Archive of the Photogrammetry, Remote Sensing and Spatial Information Sciences. Vol. XXXVII. Part B1. Beijing

Massonnet, D. and K. L. Feigl (1998). "Radar interferometry and its application to changes in the Earth's surface." Reviews of Geophysics 36(4): 441-500.

Mather P. M. , 2004, Computer processing of remotely sensed images: an introduction, John Wiley and Sons ???

Meyer, B. and K. Le Dortz, 2007, Strike-slip kinematics in Central and Eastern Iran: Estimating fault slip-rates averaged over the Holocene, TECTONICS, VOL. 26, TC5009, doi:10.1029/2006TC002073.

Motagh, M., T. R. Walter, M. A. Sharifi, E. Fielding, A. Schenk, J. Anderssohn, and J. Zschau (2008), Land subsidence in Iran caused by widespread water reservoir overexploitation, Geophys. Res. Lett., 35, L16403, doi:10.1029/2008GL033814.

Oveisgharan S., 2007, Estimation snow accumulation from InSAR correlation observation , PhD Thesis, STANFORD UNIVERSITY

Parsons, B.; T. Wright, P. Rowe, J. Andrews, J. Jackson, R. Walker, M. Khatib, M. Talebian, E. Bergman and E. R. Engdahl, (2006), The 1994 Sefidabeh (eastern Iran) earthquakes revisited: new evidence from satellite radar interferometry and carbonate dating about the growth of an active fold above a blind thrust fault, Geophys. J. Int. ; 164, 202-217

Pathier, E. (2003). Apports de l'interférométrie radar différentielle à la tectonique active de Taiwan. Laboratoire de Tectonique Univ. Paris6 / Laboratoire Geomatériaux Univ. Marne-La-Vallée. J. Angelier and B. Deffontaines, Université de Marne-la-Vallée: 272.

Peterson Erica H. , 2008, Applications and Orbit Scenarios for a Multistatic InSAR Formation Flying Microsatellite Mission, , University of Toronto

Perice J. E.,1999; Coseismic and postseismic deformation associated with the 1992 Landers, California, earthquake measured by Synthetic Aperture Radar Interferometry, Universy of California, San diego

Rosen, P. A., S. Hensley, G. Peltzer, and M. Simons (2004), Updated repeat orbit interferometry package released, Eos Trans. AGU, 85(5), 47.

Savage, J. and Burford, R., Geodetic determination of relative plate motion in Central California, J. Geophys. Res., 1973.

Scholz,C. H., Scaling laws for large earthquakes: consequences for physical models, Bull. Seismol. Soc. Am., 72,1-14,1982.

Smith L. C.,2002; Emerging applications of Interferometric Synthetic Aperture Radar(InSAR) in Geomorphology and Hydrology, Annals of Association of American Geographers, 92(3),2002, pp.385-398

Tavakoli, (2007), Present-day deformation and kinematics of the active faults observed by GPS in the Zagros and east of Iran, PhD Thesis, University Joseph Fourier Grenoble-1, France.

Tchalenko, J., Berberian, M and Behzadi, H (1973), Geomorphic and seismic evidence for recent activity of the Doruneh fault, Iran. Tectonophysics, 19, 333-341.

Vernant, P. et al., 2004. Present-day crustal deformation and plate kinematics in the Middle East constrained by GPS measurements in Iran and northern Oman, Geophys. J. Int., 157, 381–398

Walker, R. and J. Jackson, (2004) Active tectonics and late Cenozoic strain distribution in central and eastern Iran. Tectonics, 23, TC5010, 10.1029/2003TC001529.

Walker, R, J. Jackson and C. Baker. (2004), Active faulting and seismicity of the Dasht-e-Bayaz region, eastern Iran, Geophysical Journal International, 157, 265-282. Walpersdorf A. et al., NS shear kinematics across the Lut block from a dense GPS velocity field in eastern Iran, in preparation, 2010.

Wells, D.L., and K.J. Coppersmith (1994), New empirical relationships among magnitude, rupture length, rupture width, rupture area, and surface displacement, Bull. Seismol. Soc. Am., 84 (4), 974-1002.

Wright T.., Parsons B., England Philip C., Fielding Eric J., 2004, InSAR observation of low slip rates on the Major faults of Western Tibet, Science, vol. 305

Wright Tim J., Parsons B., Fielding Eric J., 2001, Measurement of interseismic strain accumulation across the North Anatolian Fault by satellite radar Interferometry, Geophysical Research Letters, Vol. 28, No. 10, pages 2117-2110

Zebker, H. A. and Goldstein, R. M. (1986). Topographic mapping from interferometric SAR observations . Journal of Geophysical Research, 91:4993–4999.

Zebker, H., P. Rosen, and S. Hensley, Atmospheric effects in interferometric synthetic aperture radar surface deformation and topographic maps, J. Geophys. Res., 102, 7,547-7,563, 1997.

7 Annex

Synthetic Aperture Radar (SAR) is a remote-sensing technique that acquires data at daylight or night and without weather limitation. It is a technique for extracting three-dimensional information of the earth's surface with high spatial sampling close to 10 m on ground, high resolution close to mm-cm using InSAR processing. This technique also has temporal resolution of 35 days to take the next image from specific area.

7.1 Resolution

Spatial resolution is the potential to distinguish different objects close to each other. The resolution of SAR images is different in azimuth and range direction. Range resolution before SAR processing depends on the pulse duration. Range resolution of side-looking image is:

$$R_R = \frac{C\tau}{2\sin\varphi} \quad (1)$$

Where τ is pulse duration, φ is incident angle and C pulse velocity

Azimuth resolution before SAR processing depends on the ratio between signal wavelength and antenna length. A small ratio provides better resolution, so it will be improved by decreasing wavelength and increasing antenna length. The azimuth resolution of a side-looking image is:

$$R_A = \frac{H\lambda}{l\cos\varphi} \quad (2)$$

Where λ is wavelength, H is altitude, φ is incident angle, l antenna length

For ENVISAT ASAR in image mode given λ= 5.6 cm, $\tau_{.}$ = 37.1 μs, l= 10 m, H = 700 km, and $\varphi_{.}$ = 23°, $\mathbf{R_R} \approx$ 4.8 km and $\mathbf{R_A} \approx$ 14 km before SAR processing.

The Synthetic Aperture Radar processing allows to dramatically enhancing the resolution in range and azimuth direction (Bamler 2000) to:

$$R_{Rsar} = \frac{c}{2B} \quad (3)$$

where B is the frequency bandwidth of transmitted pulse (16MHz for ENVISAT ASAR)

$$R_{asar} = \frac{l}{2} \quad (4)$$

which gives for ENVISAT ASAR a ground resolution of 20m in range direction and 4m in azimuth direction. Note that after SAR processing the achieved azimuth resolution is equivalent to the resolution before processing with an antenna of about 10km. actually, the SAR processing is using the displacement of the satellite to increase artificially the antenna length, and then simulates a large antenna length, 1000 times larger than the real one in the case of ENVISAT.

7.2 InSAR Image processing

The first step in SAR Image processing is the focalization (also called compression) in azimuth and range directions, which consists to apply the SAR processing to the raw complex radar signal in order to get a SAR image with a dramatic increase in resolution (see §3.2). The range Doppler algorithm is a common algorithm to compress the data. This algorithm includes 3 main steps:

- Range compression: use match filter and multiplying every raw data by this filter
- Range Cell Migration Correction: apply a shift to the range compression data
- Azimuth compression: use match filter like on the range direction
- The resulting image is called a single look complex (SLC) image.

7.2.1 Image registration

Once each image has been focused, it is necessary before computing the phase difference that the two SLC images are precisely co-registered, so that we are comparing the phases of the same part of the ground. Because images are taken from slightly different points of view and because of timing error, the two images cannot be directly co-registered even by simple translation or rotation. Image registration is done by matching one of the 2 images (slave image) in the geometry of the other (master image). The geometrical deformation model of the slave image onto the master is commonly estimated by complex cross-correlation between the two SAR images. Image registration contains of 2 main steps.

- Coarse correlation: it used cross-correlation to register two images up to one or two pixel accuracy.
- Fine correlation: It is done at sub-pixel accuracy by searching sub-pixel tie, fitting transformation equations
- Re-sampling of slave image into master image geometry is done based on the deformation model estimated from the fine correlation using algorithms like nearest neighbor, bilinear and cubic convolution. (Li Z. & Bathel J., 2008)

An accuracy of 1/10 of a pixel is required for interferometric application. .

7.2.2 Forming interferogram

Each pixel of the co-registered SLC images contains a complex number that can be expressed as:

$$C_x = A(x)e^{i\varphi(x)} \quad (6)$$

The image of the phase difference called an interferogram is generated by the complex conjugate product of the two images:

$$C_1 C_2^* = A_1 A_2 e^{i(\varphi_1 - \varphi_2)} = R(x) + iI(x) \quad (7)$$

Figure 3.6 presents the interferogram of two images with a repeat pattern that is called fringe. Each fringe in the figure indicates one phase difference cycle (2π). Each cycle contain blue, cyan, green, yellow and red with 0(blue) to 2π (red). In this step fringes are mainly related to the satellites orbit error and topography (Mather, P. M. 2004).

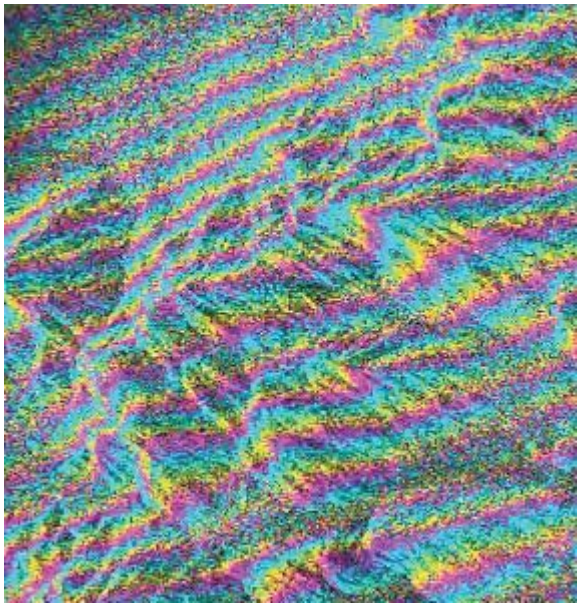

Figure 7.1: Interferogram with repeat pattern

7.2.3 Interferogram flattening

At that stage, the interferometric phase is composed of different terms related to orbital error, to topography, to atmosphere, to deformation and to noise.

$$\varphi = \varphi_{orbit} + \varphi_{topo} + \varphi_{atm} + \varphi_{def} + \varphi_{noise} \quad (8)$$

As mentioned in §3.2, if two images have exactly the same flight path, the baseline between two image will be zero, and the topographic term will be null. But in reality this effect has to be corrected.

In this step, the interferometric phase related to this geometrical effect is simulated using a DEM and precise orbits. The orbit determination is based on models of the forces acting on the satellite, where selected parameters of these models are adjusted, along with an initial satellite position and velocity. This adjustment is done in order to make the resulting orbit fit to the tracking data in a least squares sense. The most important force models include the Earth's irregular gravity field, the effects of tides on the gravity field, aerodynamic drag by the upper atmosphere, and radiation pressure forces from the Sun and Earth. Gravity effects from the Moon, Sun and planets are also taken into account. Interferogram flattening is done by subtracting the simulated interferometric phase from the initial Interferogram.

7.2.4 Phase Unwrapping

The interferometric phase varies between 0 and 2π , therefore the phase is wrapped in this range. In other words, when the signal phase reaches one of the range value boundaries (0 or 2π), it jumps to the other one (figure 3.7).

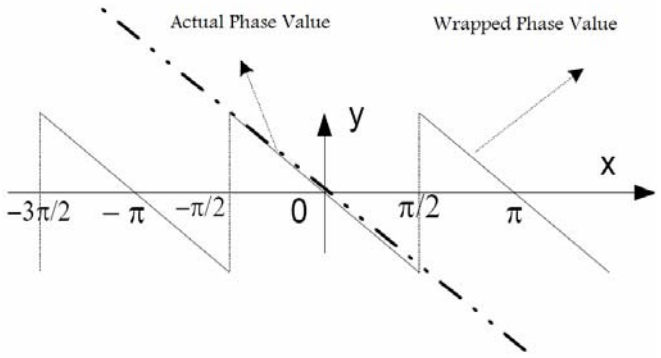

Figure 7.2: Wrapped and Unwrapped phase (from Mather P. M. 2004)

The unwrapping process has to be done in 2D and is not trivial in a real interferogram, especially when the interferometric phase is noisy. Amongst the different existing algorithms the branch-and-cut approach is quite common (Ghiglia et al. 1998):

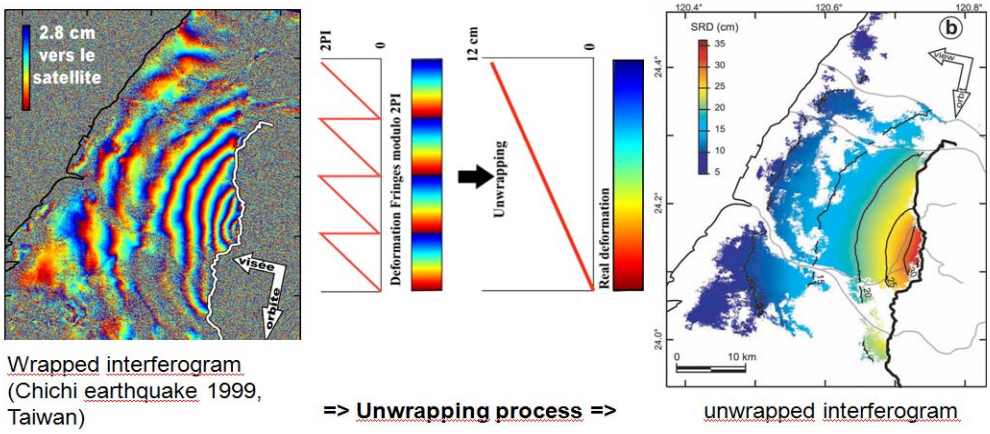

Figure 7.3: The unwrapping process (from Pathier 2003)

7.2.5 Geocoding

To interpolate the interferogram, it is necessary to convert the unwrapped phase to topographic height. In this step each pixel is transferred from radar coordinates to geo-referenced coordinates.

8 List of Figures